

# FINAL REPORT

Magnetic Surface Modes and UXO/Clutter Classification and  
Discrimination

SERDP Project MR-1658

DECEMBER 2011

Thomas Bell  
SAIC

*This document has been cleared for public release*



# REPORT DOCUMENTATION PAGE

*Form Approved  
OMB No. 0704-0188*

Public reporting burden for this collection of information is estimated to average 1 hour per response, including the time for reviewing instructions, searching existing data sources, gathering and maintaining the data needed, and completing and reviewing this collection of information. Send comments regarding this burden estimate or any other aspect of this collection of information, including suggestions for reducing this burden to Department of Defense, Washington Headquarters Services, Directorate for Information Operations and Reports (0704-0188), 1215 Jefferson Davis Highway, Suite 1204, Arlington, VA 22202-4302. Respondents should be aware that notwithstanding any other provision of law, no person shall be subject to any penalty for failing to comply with a collection of information if it does not display a currently valid OMB control number. **PLEASE DO NOT RETURN YOUR FORM TO THE ABOVE ADDRESS.**

|  |                                       |  |  |  |  |  |
|--|---------------------------------------|--|--|--|--|--|
| <b>1. REPORT DATE (DD-MM-YYYY)</b><br>3/30/2012  | <b>2. REPORT TYPE</b><br>Final Report | <b>3. DATES COVERED (From - To)</b><br>3/2009-3/2012 |  |  |  |  |
| <b>4. TITLE AND SUBTITLE</b><br><br>Magnetic Surface Modes and UXO/Clutter Classification and Discrimination<br>Discrimination   |                                       |  | <b>5a. CONTRACT NUMBER</b><br><b>09-C-0016</b>   | <b>5b. GRANT NUMBER</b>                          |  |  |
|  |                                       |  | <b>5c. PROGRAM ELEMENT NUMBER</b>  |  |  |  |
|  |                                       |  | <b>5d. PROJECT NUMBER</b><br>MR-1658   | <b>5e. TASK NUMBER</b>                           |  |  |
| <b>6. AUTHOR(S)</b><br><br>Drs. Thomas Bell and Daniel Steinhurst  |                                       |  | <b>5f. WORK UNIT NUMBER</b>  |  |  |  |
|  |                                       |  | <b>7. PERFORMING ORGANIZATION NAME(S) AND ADDRESS(ES)</b><br><br>SAIC, 4001 Fairfax Drive, Arlington VA<br>22203 | <b>8. PERFORMING ORGANIZATION REPORT NUMBER</b>  |  |  |
|  |                                       |  | <br>Nova Research, 1900 Elkin Street<br>Alexandria, VA 22308   |  |  |  |
| <b>9. SPONSORING / MONITORING AGENCY NAME(S) AND ADDRESS(ES)</b><br><br>Strategic Environmental Research and<br>Development Program  |                                       |  | <b>10. SPONSOR/MONITOR'S ACRONYM(S)</b><br>SERDP   | <b>11. SPONSOR/MONITOR'S REPORT NUMBER(S)</b>    |  |  |
|  |                                       |  |  |  |  |  |
| <b>12. DISTRIBUTION / AVAILABILITY STATEMENT</b>   |                                       |  |  |  |  |  |
| <b>13. SUPPLEMENTARY NOTES</b>   |                                       |  |  |  |  |  |
| <b>14. ABSTRACT</b><br><p>The basic objective of this research project was to develop an improved understanding of the fundamental physics underlying classification and discrimination of unexploded ordnance (UXO) and clutter items using electromagnetic induction (EMI) data. This improved understanding can help to establish a rational basis for the development and implementation of improved UXO/clutter discrimination processing and analysis techniques capable of fully exploiting the capabilities of new EMI sensor technologies purpose-built for target classification.</p> <p>We proposed to assemble a comprehensive database of EMI signatures of UXO and clutter items from a variety of active clearance sites using the ESTCP MR-200601 time domain EMI array. The objective was then to work with this library to relate the structure of the EMI signatures to the fundamental physical aspects of the EMI response arising from the magnetic surface mode and the bulk eddy current decay regimes, and establish bounds on the information content of the EMI signatures in the two regimes and their significance for UXO/clutter classification and discrimination.</p> |                                       |  |  |  |  |  |
| <b>15. SUBJECT TERMS</b>   |                                       |  |  |  |  |  |
| <b>16. SECURITY CLASSIFICATION OF:</b>   |                                       | <b>17. LIMITATION OF ABSTRACT</b>                    | <b>18. NUMBER OF PAGES</b>   | <b>19a. NAME OF RESPONSIBLE PERSON</b>           |  |  |
| <b>a. REPORT</b>   | <b>b. ABSTRACT</b>                    | <b>c. THIS PAGE</b>                                  |  | <b>19b. TELEPHONE NUMBER (include area code)</b> |  |  |

## Abstract

This research project concerns the fundamental physics of the electromagnetic response of munitions items and metallic clutter and its application to procedures for the classification of unknown buried objects using electromagnetic induction (EMI) data. The EMI response for a compact steel object exhibits an early algebraic regime wherein the response transitions from  $t^{-1/2}$  to  $t^{-3/2}$  decay, followed by a late regime characterized by an exponential decay of the response. The early, algebraic regime is associated with eddy currents confined near the surface of the object (magnetic surface modes), and its progress is described by the classical mathematics of diffusion. At late times the eddy currents have diffused throughout the object and the response decays exponentially.

An extensive database of EMI responses for munitions and clutter items was assembled for this project. The database has been used to explore the significance of the two regimes for classification. Our basic conclusion is that a decay time interval of about 0.1 ms to 3 ms is adequate for classification. This range lies within the magnetic surface mode regime for most targets of interest.

This report includes detailed descriptions of the EMI signature database, parameterization of the EMI signatures and their interpretation in terms of magnetic surface modes and exponentially decaying body modes.

## Table of Contents

|   |     |
|---|-----|
| Abstract .....  | i   |
| Table of Contents .....   | ii  |
| List of Tables .....  | iii |
| List of Figures .....   | iii |
| List of Acronyms .....  | v   |
| Keywords .....  | vi  |
| Acknowledgements .....  | vii |
| Objective .....   | 1   |
| Background .....  | 2   |
| Introduction .....  | 2   |
| Dipole Response and Polarizability .....                              | 3   |
| Magnetic Surface Modes .....  | 6   |
| Previous EMI signature data collection .....                          | 9   |
| Two Component Model .....   | 11  |
| Materials and Methods .....   | 13  |
| Data Collections .....  | 13  |
| Processing and Analysis .....   | 14  |
| Results and Discussion .....  | 16  |
| EMI Signature Library .....   | 16  |
| Mathematics of Diffusion .....  | 22  |
| Relaxation Rate Distributions .....                                   | 24  |
| Decay Time Effects on Classification Performance .....                | 28  |
| Conclusions and Implications for Future Research/Implementation ..... | 33  |
| Literature Cited .....  | 34  |

## List of Tables

|  |    |
|--|----|
| Table 1. MR-1595 target summary.....   | 10 |
| Table 2. MR-1313 target summary.....   | 10 |
| Table 3. Origin of clutter items in EMI signature library.....                     | 16 |
| Table 4. Inert munitions from live site demonstrations.....                        | 18 |
| Table 5. Additional munitions items in the EMI signature library.....              | 19 |
| Table 6. Surface and body mode time scales for Camp SLO munitions and clutter..... | 21 |

## List of Figures

|   |    |
|---|----|
| Figure 1. Basic elements of electromagnetic induction: (a) a magnetic field is produced by running current through the transmit coil, (b) when the field is cut off current eddies spring up in nearby metal objects and then quickly (~10 ms) decay, (c) the sensor measures voltage induced in receive coil by decaying magnetic field from eddy currents. .... | 2  |
| Figure 2. Principal axis polarizabilities for 4.2" mortar debris, axes as shown at right. ....  | 6  |
| Figure 3. Evolution of the magnetic field during the transient EMI response of a steel sphere....   | 6  |
| Figure 4. Measured and theoretical transient EMI response for a 2 inch steel ball. ....   | 7  |
| Figure 5. Comparison of quadrature response for a variety of compact steel targets with the magnetic surface mode function given by equation (16). ....   | 9  |
| Figure 6. Two component model fit to 60mm axial polarizability. ....  | 12 |
| Figure 7. Surface and body mode time scales from MR-1595 clutter signature library. ....  | 12 |
| Figure 8. (a) Schematic of TEMTADS array and (b) array on test stand. ....  | 13 |
| Figure 9. (a) EMI response curves measured above a 4.2 inch mortar. (b) Principal axis polarizabilities calculated by inverting the complete set of response curves. ....   | 15 |
| Figure 10. Clutter from the ESTCP live sites. ....  | 16 |
| Figure 11. Partial munitions items recovered from the Remington Woods site. ....  | 17 |
| Figure 12. Seed munitions items from Camp SLO (left) and Camp Butner (right) ....   | 18 |
| Figure 13. Principal axis polarizabilities (mean $\pm 1$ standard deviation) for Camp SLO clutter items. ....   | 20 |
| Figure 14. Principal axis polarizabilities (mean $\pm 1$ standard deviation) for Camp SLO seed munitions items. ....  | 21 |
| Figure 15. Two component model fits to 60mm mortar and 3.5" rocket body polarizabilities....  | 22 |
| Figure 16. Cole-Cole diagrams of principal axis polarizabilities for a munitions fragment recovered from the Badlands Bombing Range. ....   | 24 |
| Figure 17. Cole-Cole plots for 37mm projectiles excited axially (left) and transversely (right). Red circles correspond to an intact round, black diamonds to a round with its driving band missing. ....   | 25 |

|  |    |
|--|----|
| Figure 18. Cole-Cole relaxation time distribution compared with model amplitude distribution for a 2" diameter steel sphere.....   | 26 |
| Figure 19. Calculated 2 inch sphere response compared to Cole-Cole approximation.....  | 26 |
| Figure 20. Empirical decay time spectra for 60mm mortar (left) and exploded 4.2" mortar body (right). Top plots show Prony model fits to principal axis polarizabilities, bottom plots show corresponding relaxation time distributions..... | 27 |
| Figure 21. Scatter plot of response strength vs. fundamental mode relaxation rate from Prony fits to munitions and clutter polarizabilities.....   | 28 |
| Figure 22. Ringdown for different TEMTADS receiver coils.....  | 29 |
| Figure 23. Observed TEMTADS background variation at several sites. ....  | 29 |
| Figure 24. Signal and noise histograms at 0.1, 1.0 and 10 ms for the man-portable TEMTADS at Camp Beale.....   | 30 |
| Figure 25. Classification performance using restricted decay time ranges. ....   | 31 |
| Figure 26. Run-on effect of shortened pulse length on target signature. ....   | 32 |

## **List of Acronyms**

|         |   |
|---------|---|
| BUD     | Berkeley UXO Discriminator                                  |
| DARPA   | Defense Advanced Research Projects Agency                   |
| EMI     | Electromagnetic Induction                                   |
| ESTCP   | Environmental Security Technology Certification Program     |
| GEM     | Geophex Electromagnetic (sensor)                            |
| MR      | Munitions Response  |
| NRL     | Naval Research Laboratory                                   |
| Rx      | Receive   |
| SAIC    | Science Applications International Corporation              |
| SEM     | Singularity Expansion Method                                |
| SERDP   | Strategic Environmental Research and Development Program    |
| SLO     | San Luis Obispo   |
| SNR     | Signal to Noise Ratio                                       |
| Tx      | Transmit  |
| TEM     | Transient Electromagnetic                                   |
| TEMTADS | Transient Electromagnetic Towed Array Discrimination System |
| UXO     | Unexploded Ordnance   |

## **Keywords**

Electromagnetic induction, EMI, eddy current, munitions, clutter, classification, diffusion, magnetic surface mode, magnetic polarizability, UXO

## **Acknowledgements**

This project was a collaborative effort between Science Applications International Corporation (SAIC) and Nova Research. Dr. Daniel Steinhurst was the co-principal investigator for Nova Research. Dr. Bell was assisted by Drs. Bruce Barrow, Nagi Khadr and Jim Kingdon. Dr. Steinhurst was assisted by Mr. Glenn Harbaugh. Use of the Naval Research Laboratory's Blossom Point facility and transient electromagnetic induction array for data collection is gratefully acknowledged. This work was supported by the Strategic Environmental Research and Development Program.

## Objective

The basic objective of this research project was to develop an improved understanding of the fundamental physics underlying classification and discrimination of unexploded ordnance (UXO) and clutter items using electromagnetic induction (EMI) data. This improved understanding can help to establish a rational basis for the development and implementation of improved UXO/clutter discrimination processing and analysis techniques capable of fully exploiting the capabilities of new EMI sensor technologies purpose-built for target classification.

We proposed to assemble a comprehensive database of EMI signatures of UXO and clutter items from a variety of active clearance sites using the ESTCP MM-0601 time domain EMI array. The objective was then to work with this library to relate the structure of the EMI signatures to the fundamental physical aspects of the EMI response arising from the magnetic surface mode and the bulk eddy current decay regimes, and establish bounds on the information content of the EMI signatures in the two regimes and their significance for UXO/clutter classification and discrimination.

The results of this research should generalize directly to other EMI sensors, regardless of sensor design. The basic products are principal axis polarizabilities derived from data collected for the various UXO and clutter targets. As such they are sensor-independent, intrinsic properties of the targets. The products of this research will be useful to the user community in several ways. The signature library will be an important resource for other scientists and engineers conducting research on UXO/clutter discrimination. It will provide the necessary input for development and testing of decision rules and procedures for UXO/clutter discrimination. The results will also provide a rational basis for optimizing sensor operating parameters and data collection protocols on a site-specific basis.

## Background

### Introduction

Over the past decade or so SERDP has invested heavily in research efforts directed at developing techniques for distinguishing between buried UXO and metallic clutter items that are also found in the ground. One very important line of research centers on the EMI signatures of buried objects and ways of reliably classifying them as either ordnance-like or clutter-like. A number of SERDP projects have supported research efforts to find techniques for deciding what is ordnance-like or clutter-like about the EMI signatures. Until recently, technology limitations have hindered progress. Largely as a result of SERDP and ESTCP investments, a new generation of EMI sensors specifically designed to gather data suitable for UXO/clutter classification and discrimination has become available. Examples are the Berkeley UXO Discriminator (BUD) developed by the Lawrence Berkeley National Laboratory under SERDP project MR-1225, the transient electromagnetic (TEM) array, nicknamed “TEMTADS”, developed by the Naval Research Laboratory (NRL) in SERDP project MR-1315 and ESTCP project MR-200601, and the MetalMapper developed with funding from the Navy and SERDP project MR-1534.

These new sensors operate in the time domain. The basic elements of time domain or transient electromagnetic induction are illustrated in Figure 1. First, a magnetic field (the primary field) is produced by running a current through the transmit coil. When the transmit current is shut off the primary field shuts down, which causes current eddies to spring up in nearby metal objects. These eddy currents quickly diffuse through the object and decay, typically on a time scale of 10's of ms. The sensor measures the voltage induced in a receive coil by the decaying magnetic field (the secondary or induced field) due to the decaying eddy currents.

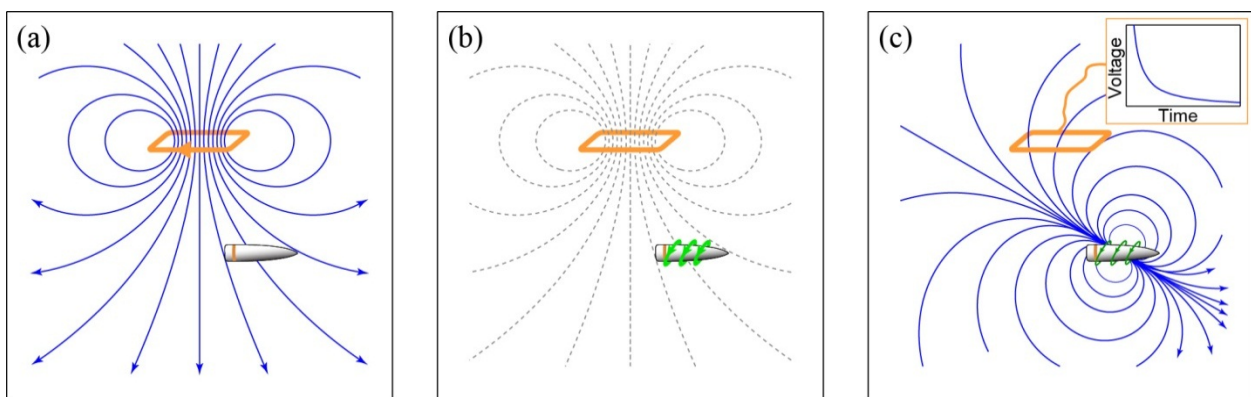


Figure 1. Basic elements of electromagnetic induction: (a) a magnetic field is produced by running current through the transmit coil, (b) when the field is cut off current eddies spring up in nearby metal objects and then quickly ( $\sim 10$  ms) decay, (c) the sensor measures voltage induced in receive coil by decaying magnetic field from eddy currents.

Purpose-built classification sensors have digitally controlled, programmable transmit waveforms and flexible receiver data recording capabilities. At present, their transmit/receive (Tx/Rx) bandwidth is set somewhat arbitrarily based on experience and expert opinion. There are a number of tradeoffs involved in selecting the bandwidth. How early after the primary field cutoff the secondary field can be measured is limited by the electronics of the sensor, but how late it is measured is to a large extent a matter of choice. The basic limitations at the late end are signal-to-noise (the signal ultimately decays exponentially) and data rate (long time measurements take a long time). The results of this research project are intended to help provide a rational basis for determining the optimum sensor bandwidth for UXO/clutter discrimination.

### Dipole Response and Polarizability

The primary field  $\mathbf{H}_0$  is produced by current flowing in the transmit coil. The relationship between the primary field and the transmit current  $I$  can be expressed in terms of a transmit coil sensitivity function  $\mathbf{C}_T$  such that

$$(1) \quad \mathbf{H}_0 = n_T \mathbf{C}_T I .$$

We have explicitly pulled out the number of turns in the coil  $n_T$  in order that the sensitivity function can be calculated as an integral around a single loop of the transmit coil using the Biot-Savart law,

$$(2) \quad \mathbf{C}_T(\mathbf{r}) = \frac{1}{4\pi} \oint \frac{d\mathbf{l}_T \times (\mathbf{r} - \mathbf{r}_T)}{|\mathbf{r} - \mathbf{r}_T|^3} .$$

Here  $\mathbf{r} - \mathbf{r}_T$  is a vector from a point on the coil  $\mathbf{r}_T$  to the field point  $\mathbf{r}$ . Changes in the primary field  $\mathbf{H}_0$  induce eddy currents in the target, which in turn produce the induced field  $\mathbf{H}_I$ . The signal  $S(t)$  is proportional to the receiver voltage  $V(t)$  created by a changing magnetic flux through the coil due to  $\mathbf{H}_I$  (Faraday's law):

$$(3) \quad S(t) \propto V(t) = - \frac{d}{dt} \int \mathbf{B}_I \cdot d\mathbf{a}_R .$$

In equation (3)  $\mathbf{B}_I = \mu_0 \mathbf{H}_I$  is the magnetic induction or flux density, where  $\mu_0 = 4\pi \times 10^{-7}$  H/m is the permeability of free space. Stokes' theorem can be used to relate the integral of the flux density  $\mathbf{B}$  ( $= \nabla \times \mathbf{A}$ ) over a surface enclosed by a loop to an integral around the loop of the corresponding magnetic vector potential  $\mathbf{A}$ , so that

$$(4) \quad V(t) = - \frac{d}{dt} \oint \mathbf{A}_I \cdot d\mathbf{l}_R .$$

We represent the effect of the eddy currents in, and magnetization of the target by an induced dipole moment  $\mathbf{m}$ , which is related to the primary field according to

(5)

$$\mathbf{m}(t) = \int \mathbf{H}_0 \mathbf{B}(t - \tau) d\tau.$$

In equation (5)  $\mathbf{B}$  is the magnetic polarizability tensor. It completely describes the induced dipole response of the target. The eigenvalues of  $\mathbf{B}$  correspond to responses induced by field components aligned with each of the target's principal axes. For a frequency-domain EMI system with  $\mathbf{H}_0(t) = \mathbf{H}_0 \exp(i\omega t)$ ,

(6)

$$\mathbf{m}(t) = \int \mathbf{H}_0 \exp(i\omega t) \mathbf{B}(t - \tau) d\tau = \mathbf{H}_0 \exp(i\omega t) \widehat{\mathbf{B}}(\omega)$$

where  $\widehat{\mathbf{B}}(\omega)$  is the Fourier transform of  $\mathbf{B}(t)$ :

(7)

$$\widehat{\mathbf{B}}(\omega) = \int \mathbf{B}(t) \exp(i\omega t) dt.$$

The vector potential at a field point  $\mathbf{r}$  due to the induced dipole moment  $\mathbf{m}$  in an object at position  $\mathbf{r}_0$  is given by

(8)

$$\mathbf{A}_I = \frac{\mu_0}{4\pi} \frac{\mathbf{m} \times (\mathbf{r} - \mathbf{r}_0)}{|\mathbf{r} - \mathbf{r}_0|^3}.$$

The receiver voltage is then

(9)

$$V(t) = - \frac{d}{dt} \frac{\mu_0}{4\pi} \oint \frac{(\mathbf{m} \times (\mathbf{r} - \mathbf{r}_0)) \cdot d\mathbf{l}_R}{|\mathbf{r} - \mathbf{r}_0|^3}.$$

Since the scalar triple product  $(\mathbf{m} \times \mathbf{r}) \cdot d\mathbf{l} = \mathbf{m} \cdot (\mathbf{r} \times d\mathbf{l}) = \mathbf{m} \cdot (d\mathbf{l} \times (-\mathbf{r}))$ , this is equivalent to

(10)

$$V(t) = - \left( \frac{\mu_0}{4\pi} \oint \frac{d\mathbf{l}_R \times (\mathbf{r}_0 - \mathbf{r}_R)}{|\mathbf{r} - \mathbf{r}_0|^3} \right) \cdot \frac{d\mathbf{m}}{dt} = -\mu_0 n_R \mathbf{C}_R \cdot \frac{d\mathbf{m}}{dt},$$

where now  $\mathbf{C}_R$  is the receiver coil sensitivity function and  $n_R$  is the number of turns in that coil. Inserting the expressions for the induced dipole moment and the primary field from equations (5) and (1), respectively, we have

(11)

$$V(t) = -\mu_0 n_R n_T \mathbf{C}_R(\mathbf{r}_0 - \mathbf{r}_R) \cdot \mathbf{C}_T(\mathbf{r}_0 - \mathbf{r}_T) \int I'(t - \tau) \mathbf{B}(\tau) d\tau.$$

For an ideal time-domain sensor (current maintained at a constant level  $I_0$  and then instantaneously returned to zero), this becomes

(12)

$$V(t) = \mu_0 n_R n_T I_0 \mathbf{C}_R \cdot \mathbf{C}_T \mathbf{B}(t).$$

Alternatively for an ideal frequency-domain measurement with  $I(t) = I_0 \exp(i\omega t)$ ,

(13)

$$V(t) = -i\omega \mu_0 n_R n_T I_0 \mathbf{C}_R \cdot \mathbf{C}_T \hat{\mathbf{B}}(\omega) \exp(i\omega t).$$

Equations (11) - (13) each include three basic terms:

1. A normalization factor  $\mu_0 n_R n_T I_0$ , with or without the  $i\omega$ , that depends only on the transmit and receive electronics,
2. The coil sensitivity functions  $\mathbf{C}_R$  and  $\mathbf{C}_T$  that depend only on geometry and the target location relative to the sensor, and
3. The polarizability tensor  $\mathbf{B}(t)$ , or its Fourier transform  $\hat{\mathbf{B}}(\omega)$ , which depends only on the target and its orientation.

The eigenvalues  $\beta_i$ ,  $i = 1, 2, 3$ , of the polarizability tensor are referred to as the principal axis polarizabilities of the target. They correspond to decaying (or oscillating) dipole moment components induced by unit strength primary field components along each of the target's three principal axis directions. The principal axis polarizabilities depend on the size, shape and composition of the target. They contain all of the information about the target's EMI response that is useful for target identification or classification.

Given a set of measurements of the target response with varying geometries or "look angles" such that the corresponding coil response functions  $\mathbf{C}_T$  and  $\mathbf{C}_R$  cover a full complement of directions at the target, the data can be inverted to determine the location of the target, the orientation of its principal axes, and the three principal axis polarizabilities [1].

Figure 1 shows the principal axis polarizabilities for an exploded 4.2" mortar body or "halfshell" extracted from data collected using the NRL TEM array [2]. The units of polarizability here are meters<sup>3</sup> normalized by the peak transmit current in Amperes. The corresponding principal axis directions are shown superimposed on a picture of the target at the right. Clutter items often have a decidedly three-dimensional shape and three distinct polarizabilities. Typical munitions items are axially symmetric, with a degenerate pair of equal polarizabilities for directions transverse to the symmetry axis.

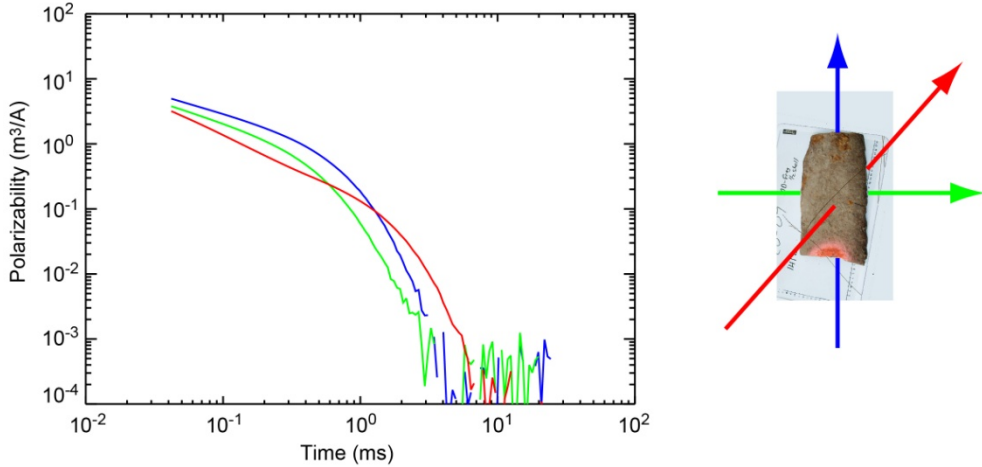


Figure 2. Principal axis polarizabilities for 4.2" mortar debris, axes as shown at right.

### Magnetic Surface Modes

A basic theoretical framework for analyzing EMI responses follows from results of SERDP project MR-1311. In that project, Weichman described how the EMI response for a compact steel object exhibits an early algebraic regime wherein the response transitions from  $t^{-1/2}$  to  $t^{-3/2}$  decay, followed by a late regime characterized by an exponential decay of the response [3]. During the early time  $t^{-1/2}$  to  $t^{-3/2}$  transition region the EMI response is dominated by eddy currents near the surface of the object, while in the late stage the response is dominated by exponentially decaying bulk or body eddy current modes. Weichman relates the early time algebraic response to the evolution of magnetic surface modes.

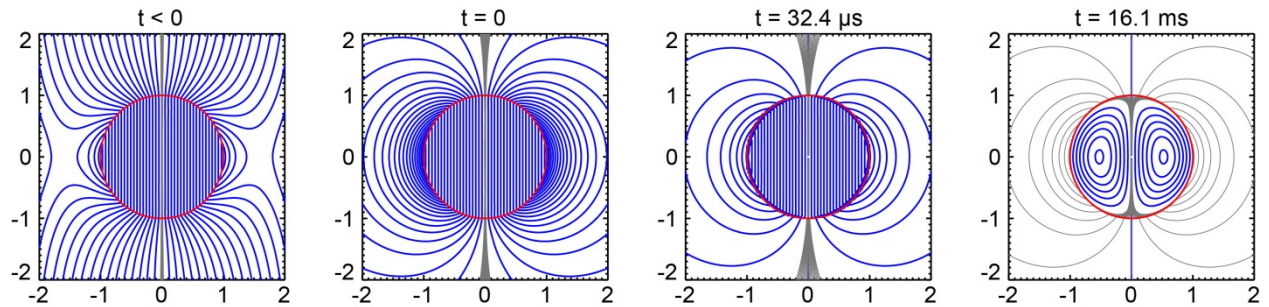


Figure 3. Evolution of the magnetic field during the transient EMI response of a steel sphere.

The diffusion of the induced eddy currents from the surface to the interior and the corresponding secondary field evolution are conveniently illustrated by the transient EMI response of a steel sphere [4, §10.08]. Figure 3 shows the evolution of the magnetic field during the response of a 2 inch diameter (radius  $a = 0.0254$  m) steel sphere with nominal conductivity and (relative) permeability values of  $\sigma = 4.0 \times 10^6$  S/m and  $k = 100$ , respectively. (The object's magnetic permeability is  $\mu = k\mu_0$ ). The field strength is proportional to the density of the field lines shown

in blue. Finely spaced gray lines are included to highlight the late stage decay detail (flux between gray lines is 2% of the flux between the blue lines).

Initially ( $t < 0$ ) the sphere is in a uniform primary field. It is magnetized, concentrating the flux of magnetic field (primary field lines would be vertical with uniform spacing without the object). When the primary field shuts off at  $t = 0$  the material cannot respond immediately and the field remains the same inside the object. Eddy currents form at the surface to balance field differences across the material boundary. The field lines loop around the surface currents, bending sharply at the edge then curving around outside and re-entering the sphere. In the magnetic surface mode regime  $t \sim t_s = \sigma\mu a^2/k^2$  (32.4  $\mu$ s in this example) the field is essentially unchanged throughout most of the object. The eddy currents have diffused into the near-surface layer. The induced secondary field outside the object decays algebraically as eddy currents spread out and weaken. In the body mode regime  $t \sim t_B = \sigma\mu a^2$  (we show the response at the fundamental body mode time scale  $t_0 = t_B/\lambda_0^2 = 16.1$  ms, where  $\lambda_0 = 4.49$  is the fundamental mode eigenvalue) the interior field lines loop around eddy currents which have diffused into the interior of the object. The secondary field is very weak (gray lines) and decays exponentially as the eddy currents die out.

Figure 4 shows the measured transient EMI response for the 2 inch steel ball and the corresponding response calculated from theory using the nominal conductivity and permeability. The response was measured using one of the sensors from the NRL TEM array with the ball situated on the sensor axis at a range of 20 cm. Over most of the measured decay time the response is algebraic, finally rolling over to exponential after a few 10's of ms. Note the subtle variation in slope between 0.01 ms and 1.0 ms.

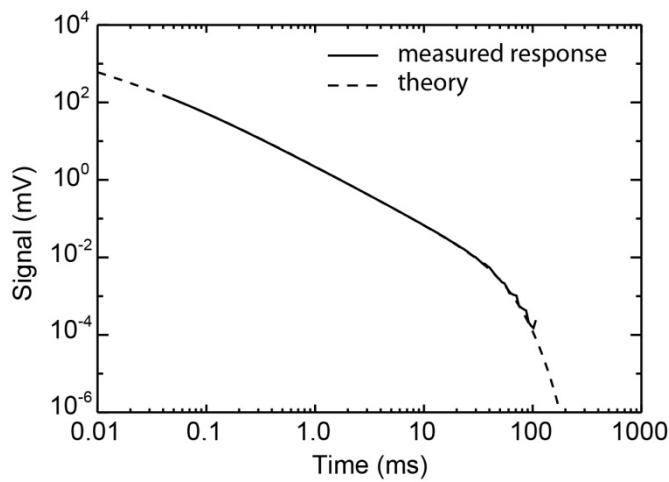


Figure 4. Measured and theoretical transient EMI response for a 2 inch steel ball.

So long as the eddy currents are confined near the surface and are not influenced by the finite thickness of the material, the secondary magnetic field follows

(14)

$$H(t) \sim \exp(v^2 t) \operatorname{erfc}(v\sqrt{t})$$

with  $v = 1/\sqrt{t_s} = k/a\sqrt{\sigma\mu}$ . The TEM sensor responds to  $\partial H/\partial t$  over the receive loop, and

(15)

$$-\frac{\partial H}{\partial t} \sim \frac{1}{\sqrt{\pi t}} - v \exp(v^2 t) \operatorname{erfc}(v\sqrt{t})$$

which behaves as  $t^{1/2}$  for  $t \ll t_s$  and  $t^{3/2}$  for  $t \gg t_s$ . Equations (14) and (15) describe the magnetic surface mode response that was derived by Weichman, with parameter  $v$  given by the local surface mode eigenvalue.

In the frequency domain the corresponding response is given by the Fourier transform of equation (15),

(16)

$$H(\omega) \sim \frac{-1}{v + (i\omega)^{1/2}}$$

[5, 6]. The real part of the frequency domain response is in phase with the primary field, and the imaginary part is 90° out of phase (in quadrature). The peak quadrature response occurs at  $\omega = 2\pi f = v^2$ . Equation (16) was found to provide a reasonably good representation of the response near the peak of the quadrature spectrum for a variety of compact steel objects [7]. This is illustrated in Figure 5 which is a composite of 58 measured quadrature spectra of a variety of inert ordnance items, plates, cylinders, I-beam pieces, etc. that were used in Phase IV of the Jefferson Proving Ground Technology Demonstration Program [8]. For each of the targets, the response was measured with the GEM-3 [9] at frequencies of 30, 90, 210, 510, 1350, 3570, 9210, and 23970 Hz. The spectra are normalized to the quadrature peak. Individual data points correspond to values of the response normalized by the peak quadrature response for that target, with  $v^2$  equal to  $2\pi$  times the frequency at which the quadrature peak occurs. The solid curve is  $2(1+\sqrt{2})v$  times the imaginary part of equation (16) which brings the amplitude of the surface mode function to unity at the peak at  $\omega/v^2 = 1$ .

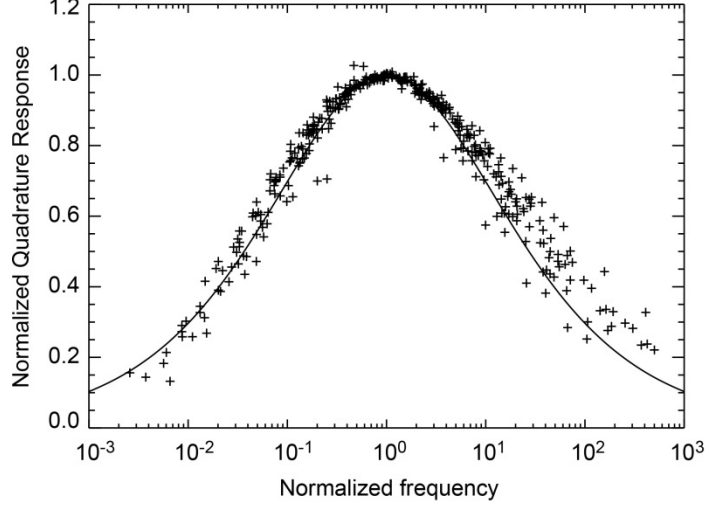


Figure 5. Comparison of quadrature response for a variety of compact steel targets with the magnetic surface mode function given by equation (16).

### Previous EMI signature data collection

The predecessor to this project was SERDP project MR-1595 [10]. An inventory of almost 1000 clutter items recovered from various cleanup sites was assembled for that project. The clutter items included exploded ordnance fragments from the Badlands Bombing Range in Pine Ridge, South Dakota, cultural clutter items recovered from the Lake Success redevelopment project in Bridgeport, Connecticut (site of a former Remington Arms plant, also known as Remington Woods), range scrap recovered from Fort A.P. Hill as part of the Defense Advanced Research Projects Agency (DARPA) backgrounds study [11] and a variety of exploded ordnance fragments, range scrap and cultural clutter recovered from former Camp Sibert in Alabama for the first of the ESTCP Classification Pilot Program Live Site Demonstrations. Table 1 gives a summary. Time domain signature data were collected for the entire library using the NRL array. A representative subset of the library items was also measured using the GEM-3 sensor. All of the data were inverted using the standard dipole response model described above to extract principal axis polarizabilities for the objects.

In SERDP project MR-1313, we assembled a database of time domain (Geonics EM-63) and frequency domain (GEM-3) EMI response measurements for a number of inert munitions items that had been recovered at Jefferson Proving Ground, Fort McClellan, Fort Ord and the Blossom Point Proving Ground in Maryland [12]. Table 2 gives a summary. EMI responses were measured along the nominal principal axis directions – parallel to and perpendicular to the length of the UXO item. The targets were split up into distinct groups based on ordnance type and model, and sample statistics were calculated for target signal parameters within each group in order to assess the inherent target signature variability. Because of the large variety of subcategories of UXO types, a total of 92 groups were analyzed. Most of the groups had

relatively few targets: seventeen had at least ten samples, but only four had at least twenty. Confidence intervals on the estimates of the means and standard deviations of the target parameters were estimated using Jackknife and Bootstrap re-sampling procedures. Typically, we found that 10-30 target samples were needed to get error bars of  $\pm 33\%$ . Table 2 lists the targets that were measured in MR-1313.

| Site         | Target Type           | Number |
|--------------|-----------------------|--------|
| Camp Sibert  | Halfshell             | 63     |
|              | Base plate            | 91     |
|              | Nose frag.            | 97     |
|              | Misc. frag & cultural | 552    |
|              | Total                 | 803    |
| Other Sites* |                       | 193    |
| Total        |                       | 996    |

\* Fort A.P. Hill (range scrap), Badlands Bombing Range (frag), former Remington Arms plant (cultural)

Table 1. MR-1595 target summary.

| Target           | Number | Target           | Number |
|------------------|--------|------------------|--------|
| 20mm projectile  | 27     | 2.36 inch rocket | 30     |
| 25mm projectile  | 4      | 3 inch Stokes    | 36     |
| 37mm projectile  | 46     | 3.5 inch rocket  | 68     |
| 40mm projectile  | 24     | 4 inch Stokes    | 35     |
| 57mm projectile  | 5      | 4.2 inch mortar  | 2      |
| 60mm mortar      | 50     | hand grenade     | 40     |
| 75mm projectile  | 14     | rifle grenade    | 27     |
| 81mm mortar      | 79     | fuze             | 73     |
| 90mm projectile  | 14     | flare            | 17     |
| 105mm projectile | 5      | other            | 47     |
| 155mm projectile | 21     | Total            | 664    |

Table 2. MR-1313 target summary.

Although useful, these EMI signature libraries are incomplete. The MR-1313 munitions signature database only provides the shape of the response for the targets' principal axes, not the actual principal axis polarizabilities. Clutter tends to be site-specific, and the MR-1595 clutter signature library is dominated by items recovered from Camp Sibert. A major goal of this (MR-1658) project was to expand the EMI signature database to include EMI signatures for a wider variety of clutter items and a good cross-section of munitions types.

## Two Component Model

A two-component surface/body mode model for fitting principal axis polarizability data was developed in MR-1595. The basic idea was to use a representation that interpolates between an early time algebraic response based on Weichman's surface mode and a late time exponential response.

We expect the magnetic surface mode response given by equation (15) to apply locally in different areas of the target's surface, with the local  $t_S$  depending on the surface curvature of the target in that area. The sphere response follows equation (15) exactly in the magnetic surface mode regime because there is only one characteristic length scale associated with the surface curvature. For a compact, but not spherical object we expect that the response in the region will be somewhat distorted, although it should retain the asymptotic  $t^{-1/2}$  and  $t^{-3/2}$  limiting behavior. To accommodate this, we use a generalized parametric form

(17)

$$\beta_{\text{early}} = \frac{A_S}{(t/t_S)^{1/2}[1 + (t/t_S)^\gamma]^{1/\gamma}}$$

with an effective surface mode time scale  $t_S$  that corresponds to some average over the entire object and a parameter  $\gamma$  that controls the width of the  $t^{-1/2}$  to  $t^{-3/2}$  transition regime. For late times, we fit to a simple exponential

(18)

$$\beta_{\text{late}} = A_B \exp(-t/t_0).$$

The basic idea is to fit the response to equation (17) from the front until the data starts to diverge from the model, then fit to equation (18) from the back until the data and model diverge, and finally interpolate between the two. Figure 6 is an example, showing the axial polarizability for a 60mm mortar and the fit using the two component model. Symbols show the polarizability determined from data collected with the NRL TEM array, and curves show the early (surface mode) and late (body mode) parametric fits to the measured response. The fit to the early time response starts out solid, then changes to dashed as the actual polarizability starts to diverge from algebraic behavior. The exponential fit to the late time response ends up solid, but is shown dashed in the region where the polarizability is better represented by the algebraic form. The transition from algebraic to exponential decay is fairly rapid, so the two solid curves appear continuous in these plots.

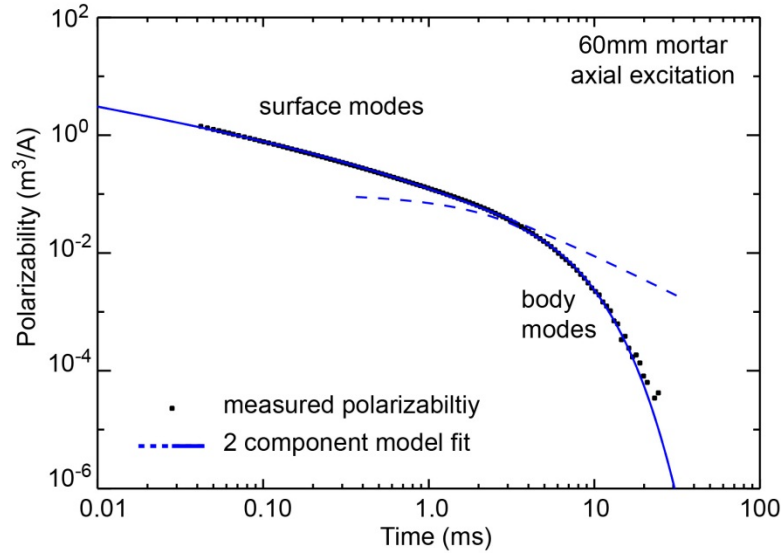


Figure 6. Two component model fit to 60mm axial polarizability.

Distributions of surface and body mode time scales for clutter items in the MR-1595 signature library are shown in Figure 7. The histograms on the left show distributions of surface mode and body mode time scales taken separately. They are plotted only over the range from 0.04 ms to 25 ms, corresponding to the EMI decay range measured by the NRL array. As it turns out, the array only resolves the surface mode time scale for about  $\frac{1}{2}$  of the clutter polarizabilities. The other half have at least one surface mode time scale that is too small to be determined by fitting the TEM data with the two-component model, so the data tend to be censored as the surface mode time scale approaches 0.04 ms. The body mode time scale is resolved for almost all of the data. The scatter plot on the right shows the joint distribution of the time scales.

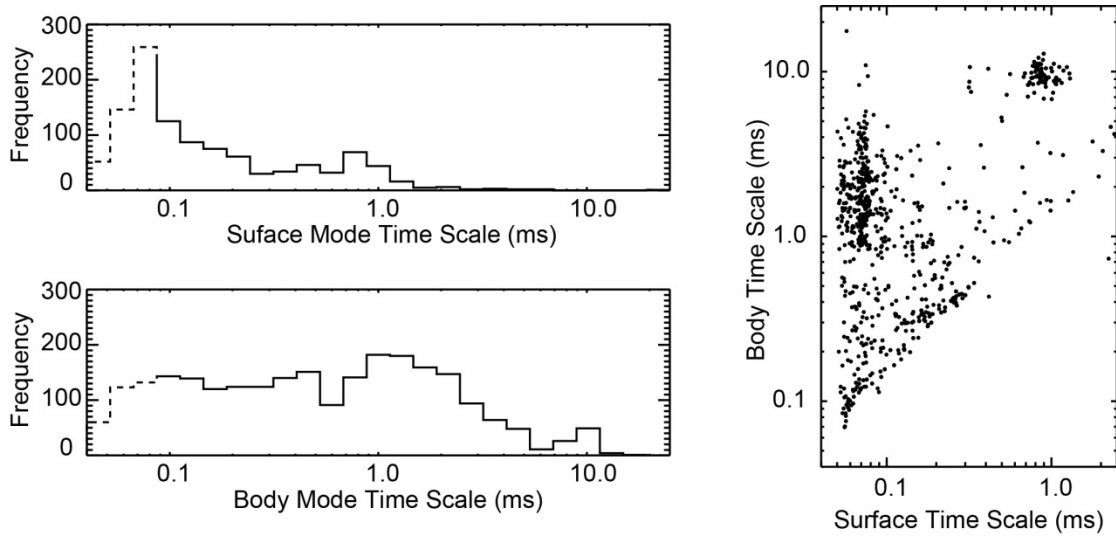


Figure 7. Surface and body mode time scales from MR-1595 clutter signature library.

## Materials and Methods

### Data Collections

An important aspect of this project was expanding the EMI signature library started in SERDP project MR-1595 to include clutter items recovered from additional active clearance sites and a representative sampling of munitions items. All of the items were shipped to NRL's test facility in Blossom Point, MD and measured using the ESTCP MR-200601 time domain EMI array. It is the business end of NRL's transient EM towed array discrimination system (TEMTADS), comprising 2x2 meter square array of 25 transmit/receive (Tx/Rx) coil pairs. The configuration is shown schematically in Figure 8(a). The Tx/Rx pairs consist of concentric 35 cm square transmit coils (shown in red in the diagram) and 25 cm square receive coils (shown in blue). The transient EMI responses of the test items were measured from 0.04 ms to 25 ms after the primary field cutoff. Figure 8(b) shows the array atop the test stand used for the EMI signature measurements.

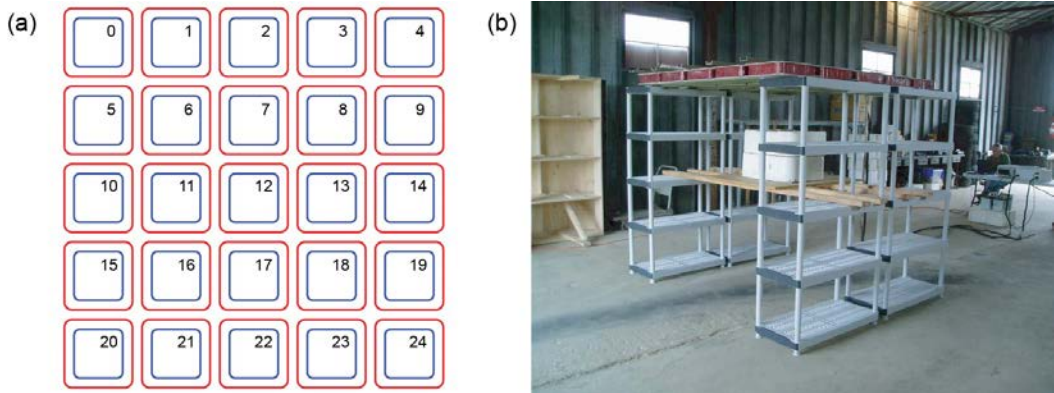


Figure 8. (a) Schematic of TEMTADS array and (b) array on test stand.

EMI signature data were collected for inert munitions and clutter items recovered from four of the ESTCP Classification Pilot Program Live Site Demonstrations sites (former Camp San Luis Obispo, former Camp Butner, former Camp Beale, Pole Mountain Target and Maneuver Area). Signature data for items from the former Camp Sibert demonstration were collected under the previous SERDP project MR-1595. We also collected signature data for a variety of clutter items recovered following the TEMTADS man-portable adjunct (ESTCP project MR-200909 [13]). demonstration at the former Remington Arms site in Bridgeport, CT, along with miscellaneous inert munitions from various sources. All of the data were inverted using the standard dipole response model to obtain principal axis polarizabilities.

The EMI response measurements were made in air with the targets supported on foam blocks below the TEMTADS array. Background (no target) signal levels were periodically measured during data collection and subtracted from target-present measurements. Because of the extremely large conductivity contrast between soil and typical munitions and clutter ( $\sim 1$  S/m vs.

$10^6$  S/m), target signatures measured in air are indistinguishable from the signatures of objects buried in the ground.

## Processing and Analysis

The data were processed to obtain principal axis polarizabilities using standard dipole inversion. The basic idea is to search out the target location, orientation and principal axis polarizabilities that minimize the difference between the measured responses and those calculated using the dipole response model described by equation (11). With some variations in the details, this approach has been used by a number of research groups in developing procedures to classify buried objects on the basis of their EMI response.

For the NRL array data, inversion is accomplished by a two-stage method. In the first stage, the target's (X, Y, Z) dipole location beneath is solved for non-linearly. At each iteration within this inversion, the nine element polarizability tensor (**B**) is solved linearly. We require that this tensor be symmetric; therefore, only six elements are unique. Initial guesses for X and Y are determined by a signal-weighted mean. The routine loops over a number of initial guesses in Z, keeping the result giving the best fit as measured by the chi-squared value. The non-linear inversion is done simultaneously over all time gates, such that the dipole (X, Y, Z) location applies to all decay times. At each time gate, the eigenvalues and angles are extracted from the polarizability tensor.

In the second stage, six parameters are used: the three spatial parameters (X, Y, Z) and three angles representing the yaw, pitch, and roll of the target (Euler angles  $\psi$ ,  $\theta$ ,  $\phi$ ). Here the eigenvalues of the polarizability tensor are solved for linearly within the 6-parameter non-linear inversion. In this second stage both the target location and its orientation are required to remain constant over all time gates, consistent with the basic dipole response construct. The value of the best fit X, Y, and Z from the first stage, and the median value of the first-stage angles are used as an initial guess for this stage. Additional loops over depth and angles are included to better ensure finding the global minimum.

Figure 9 gives an example for a munitions item. Figure 9(a) shows EMI response curves measured with the NRL array 49 cm above a 4.2 inch mortar. (Only those response curves with a peak signal greater than 5 mV are plotted.) Figure 9(b) shows the principal axis polarizabilities calculated by inverting the complete set of NRL array data. Here, the red curve is the axial polarizability and the blue and green curves are transverse polarizabilities.

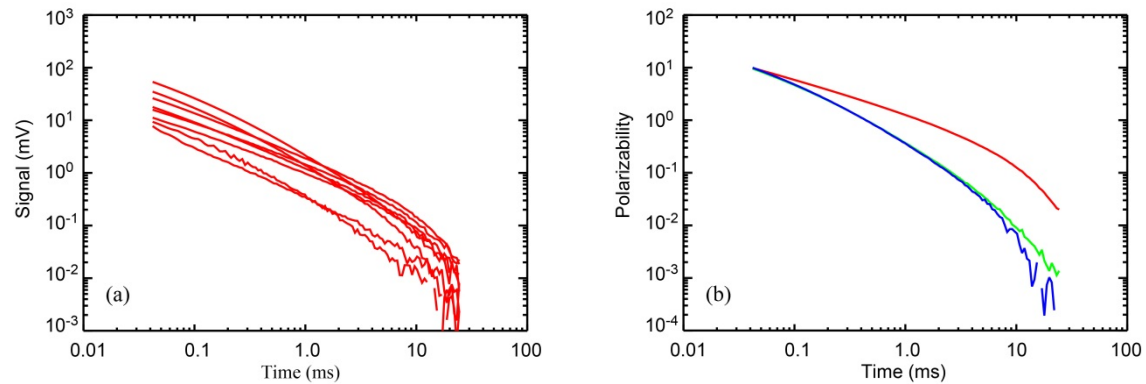


Figure 9. (a) EMI response curves measured above a 4.2 inch mortar. (b) Principal axis polarizabilities calculated by inverting the complete set of response curves.

## Results and Discussion

### EMI Signature Library

A total of 2154 clutter items were measured during this project. Table 3 gives a summary. The majority (1663) are from four sites used in the ESTCP Classification Pilot Program Live Site Demonstrations: former Camp San Luis Obispo (Camp SLO) in California, former Camp Butner in North Carolina, former Camp Beale in California, and the Pole Mountain Target and Maneuver Area in Wyoming. Recall that 823 clutter items from former Camp Sibert were measured for SERDP project MR-1595.

| Site                 | Number | Type                         |
|----------------------|--------|------------------------------|
| Camp San Luis Obispo | 700    | Cultural & munitions debris  |
| Camp Butner          | 448    | Cultural & munitions debris  |
| Camp Beale           | 208    | Cultural & munitions debris  |
| Pole Mountain        | 307    | Cultural & munitions debris  |
| Remington Woods      | 475    | Cultural & industrial debris |
| Fort Bliss           | 16     | Mortar fin pieces            |
| Total                | 2154   |                              |

Table 3. Origin of clutter items in EMI signature library.

The clutter from Camp SLO included a lot of mortar and rocket debris (Figure 10, left). The other ESTCP live sites had significantly more exploded ordnance fragments. Examples are shown in the photographs on the right in Figure 10.



Figure 10. Clutter from the ESTCP live sites.

The Remington Woods site is a Brownfields Redevelopment project in Bridgeport, CT. It is the site of a former Remington Arms plant where various small arms and explosive projectiles were manufactured and tested. Several ESTCP and SERDP projects (MR-200108, -200909, -1310)

have used the site for testing and demonstrations. The clutter is mostly cultural and industrial debris, but does include fragments and partial or broken explosive projectiles. Figure 11 shows examples of partial 37mm, 47mm and 57mm projectiles recovered from the site which are included in our signature library.

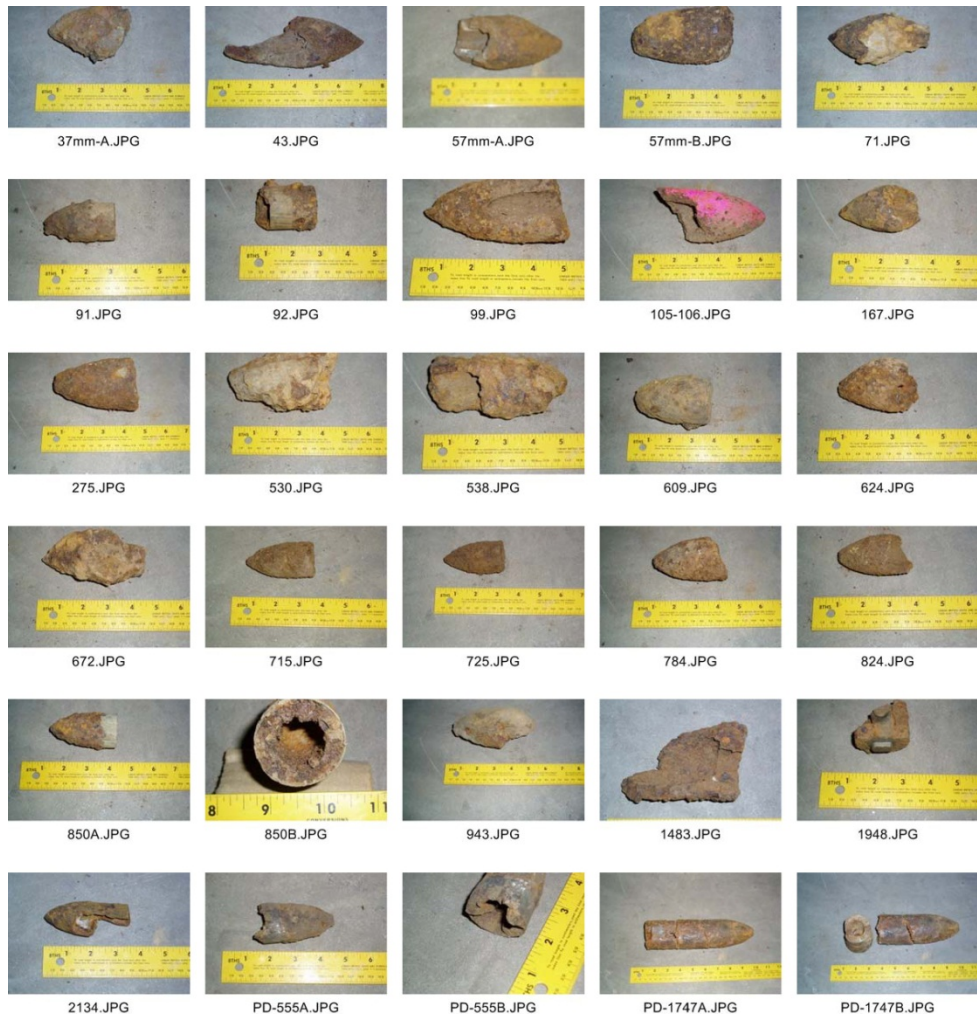


Figure 11. Partial munitions items recovered from the Remington Woods site.

A barrel of mortar tail fin debris from Camp Wheeler was provided by the U.S. Army Engineering and Support Center, Huntsville. Only a few of the items were measured because a representative sample of similar items from Camp SLO had already been measured.

Because only a very small fraction of the objects at most munitions cleanup sites are actually unexploded ordnance, the ESTCP live sites were seeded with inert munitions to improve classification statistics. Seeds from Camp SLO and Camp Butner were measured as part of this project, along with a number of inert 37mm projectiles recovered from Fort Ord in California and inert 20mm projectiles from Fort Bliss in Texas. Table 4 gives a summary of those items measured for the EMI signature library.

| Type             | Number | Source            |
|------------------|--------|-------------------|
| 20mm projectile  | 52     | Fort Bliss        |
| 37mm projectile  | 92     | Camp Butner seeds |
| 37mm projectile  | 35     | Fort Ord          |
| 2.36" rocket     | 14     | Camp SLO seeds    |
| 60mm mortar      | 14     | Camp SLO seeds    |
| 81mm mortar      | 16     | Camp SLO seeds    |
| 4.2" mortar      | 56     | Camp SLO seeds    |
| 105mm projectile | 2      | Camp Butner seeds |

Table 4. Inert munitions from live site demonstrations.

All of the available 20mm projectiles, 2.36" rockets and 4.2" mortars, and most of the 37mm projectiles had been excavated at live sites and rendered inert. They were in varying states of condition. Figure 12 shows some examples of these items. The 61mm and 81mm mortars, the 105mm projectiles (tank and howitzer) and some of the 37mm seeds were unfired inert rounds. We only measured representative samples of those items.



Figure 12. Seed munitions items from Camp SLO (left) and Camp Butner (right)

In addition to the live site demo seed munitions we have measured 44 additional inert, unfired munitions items acquired by NRL by in connection with other projects. They are listed in Table 5. Most of these items were measured at several different orientations relative to the array. This can be important for the largest items (105mm and 155mm) and for large composite items like the 81mm mortar. We have observed that when such items are not far from the sensors the dipole approximation starts to break down and the signatures may vary somewhat with orientation.

| Munition Type      | Variants | Munition Type       | Variants |
|--------------------|----------|---------------------|----------|
| <u>Projectiles</u> |          | <u>Rockets</u>      |          |
| 20mm               | 4        | 2.36"               | 2        |
| 25mm               | 2        | 2.75"               | 3        |
| 37mm               | 6        | <u>Other</u>        |          |
| 40mm               | 2        | Mk 23 practice bomb | 1        |
| 57mm               | 1        | Mk II grenade       | 1        |
| 75mm               | 2        | 40mm rifle grenade  | 1        |
| 105mm              | 3        | BDU-28              | 1        |
| 155mm              | 2        | BDU-33              | 2        |
| <u>Mortars</u>     |          | M42                 | 1        |
| 60mm               | 2        | BLU-26              | 1        |
| 81mm               | 2        | Mk 118 Rockeye      | 1        |
| 3" Stokes          | 1        |                     |          |
| 4.2"               | 2        |                     |          |

Table 5. Additional munitions items in the EMI signature library.

All of the EMI response data has been inverted to principal axis polarizabilities for the targets in the library. The Camp SLO munitions and clutter provide a representative cross section of the items in our inventory. Figure 13 shows the principal axis polarizabilities for various groups of clutter items from Camp SLO. Mean values for each group are shown by the symbols and  $\pm 1$  standard deviation about the mean by the vertical gray lines. Principal axis polarizabilities for the Camp SLO munitions seeds are shown in Figure 14. Surface and body mode time scales determined from two component model fits to the average polarizabilities for these groups are listed in Table 6. Recall that at early times the response is due to eddy currents near the surface of the object. The signal decays algebraically, slowly evolving from  $t^{-1/2}$  to  $t^{-3/2}$ . The surface mode time scale marks the center of this transition region. As the eddy currents diffuse throughout the object the signal falls off more rapidly. The late time response is an exponential decay at the body mode time scale. The surface mode time scale depends on the size and shape of the object, and how it is oriented relative to the exciting field. For typical munitions items, the surface mode time scale is significantly different depending on whether the object is excited along its axis or perpendicular to it, with axial time scale  $\gg$  transverse time scale. The body mode time scale depends primarily on the material thickness of the object, and does not depend strongly on orientation. Figure 15 shows the two component model fits for the 60mm mortars (left) and the 3.5" rocket bodies (right). The rocket bodies have a much larger length to diameter aspect ratio than the 60mm mortars (see inset pictures), which is reflected in the two component model fits. Relative to the mortars, the rocket bodies have an extended transition from the early time (surface mode) regime to the late stage decay (body mode) regime.

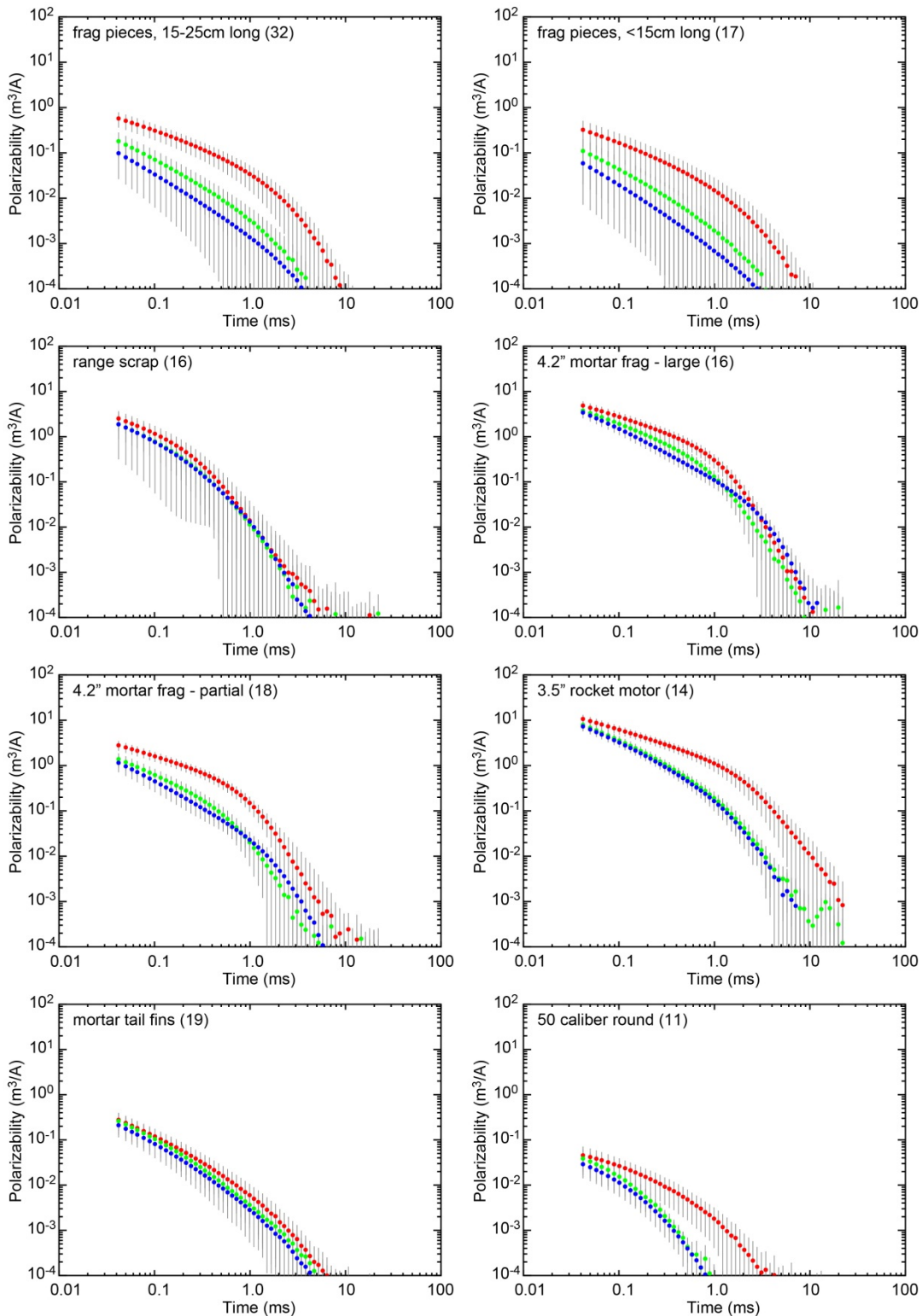


Figure 13. Principal axis polarizabilities (mean  $\pm 1$  standard deviation) for Camp SLO clutter items.

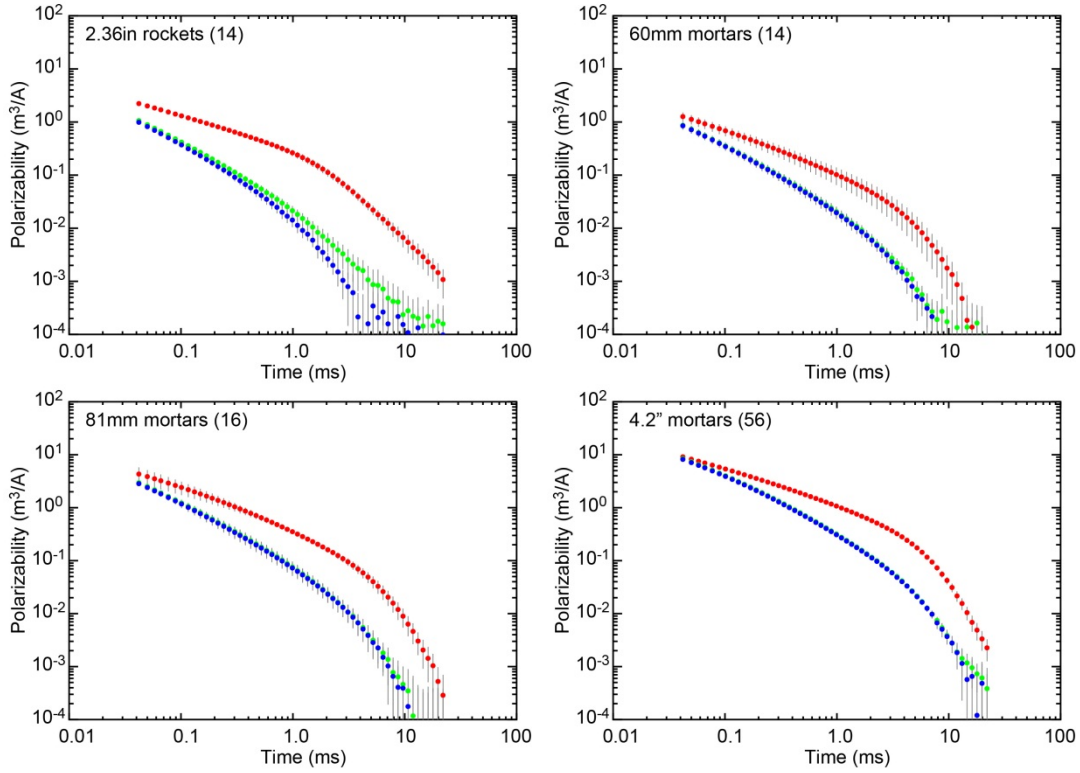


Figure 14. Principal axis polarizabilities (mean  $\pm 1$  standard deviation) for Camp SLO seed munitions items.

| Type                    | Surface mode (ms) |           |           | Body mode (ms) |           |           |
|-------------------------|-------------------|-----------|-----------|----------------|-----------|-----------|
|                         | $\beta_1$         | $\beta_2$ | $\beta_3$ | $\beta_1$      | $\beta_2$ | $\beta_3$ |
| 60mm mortar             | 1.211             | 0.081     |           | 2.64           | 1.81      |           |
| 81mm mortar             | 1.313             | 0.124     |           | 3.01           | 1.61      |           |
| 4.2" mortar             | 2.120             | 0.169     |           | 3.24           | 2.36      |           |
| 2.36" rocket            | 1.006             | 0.063     |           | 7.07           | 1.46      |           |
| Projectile frag (large) | 0.244             | 0.096     | 0.062     | 1.36           | 0.88      | 1.06      |
| Projectile frag (small) | 0.239             | 0.064     | -         | 1.52           | 0.92      | -         |
| Range scrap             | 0.086             | 0.072     | 0.069     | 1.37           | 0.50      | 0.69      |
| Mortar frag (large)     | 0.379             | 0.199     | 0.104     | 1.07           | 0.93      | 1.38      |
| Mortar frag (small)     | 0.318             | 0.106     | 0.058     | 1.38           | 0.50      | 0.89      |
| 3.5" rocket body        | 0.874             | 0.108     |           | 4.54           | 1.17      |           |
| Mortar fins             | 0.094             | 0.068     |           | 1.35           | 1.37      |           |
| 50 cal rounds           | 0.195             | 0.060     |           | 1.66           | -         |           |

Table 6. Surface and body mode time scales for Camp SLO munitions and clutter.

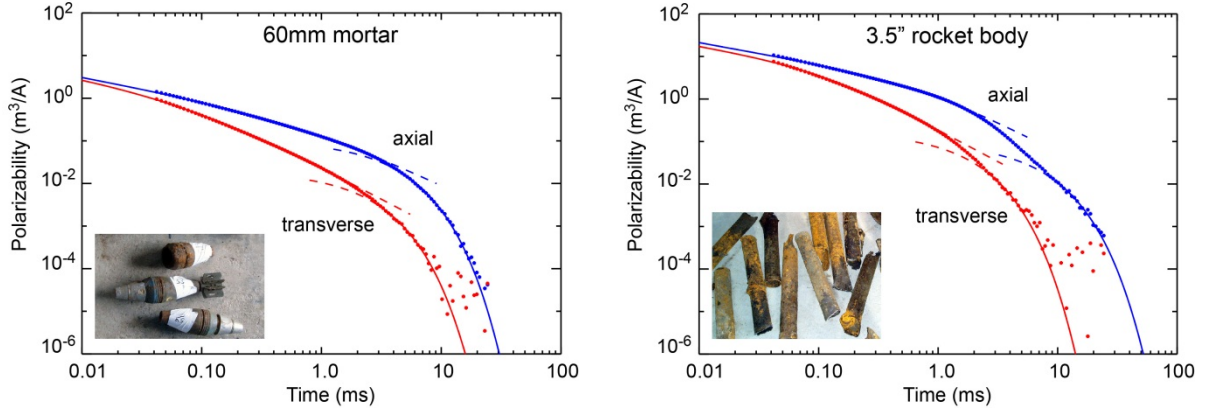


Figure 15. Two component model fits to 60mm mortar and 3.5" rocket body polarizabilities.

### Mathematics of Diffusion

With metal objects at typical EMI frequencies (<100 kHz), displacement currents associated with changing electric flux density can be neglected compared to conduction currents, and the EMI process is basically one of diffusion [14, §58]. The magnetic field inside the object obeys a vector diffusion equation

(19)

$$\frac{\partial \mathbf{H}}{\partial t} - \frac{1}{\sigma\mu} \nabla^2 \mathbf{H} = 0 .$$

wherein  $1/\sigma\mu$  serves as the diffusivity or diffusion coefficient  $D$ . Weichman [3] used a formal two-scale expansion to solve the boundary value problem for the vector diffusion equation to reveal how the early time EMI response of a highly permeable object separates into two distinct power law regimes, with the early-early time  $t^{-1/2}$  behavior crossing over to  $t^{-3/2}$  at late-early time. His early time solution for the magnetic field is given by equation (14) and repeated here

(14)

$$H(t) \sim \exp(v^2 t) \operatorname{erfc}(v\sqrt{t}) ,$$

for which  $\partial H/\partial t$  behaves as  $t^{-1/2}$  for  $t \ll 1/v^2$  and as  $t^{-3/2}$  for  $t \gg 1/v^2$ . In general a spectrum of surface wave modes may be excited, with the surface wave mode eigenvalues  $v$  depending locally on the characteristic length scales of the object. For example, the early time transient eddy current response of a driver pickup probe over a steel plate can be expressed as an integral over a continuous spectrum of these surface modes [15].

The field evolution expressed in equation (14) can also be recovered directly from simple diffusion laws with boundary conditions corresponding to evaporation or Newtonian cooling at the object's surface [16, §3.3.1, 17, §2.7]. The parameter  $v$  is then proportional to the surface

transfer coefficient  $h$  according to  $v = h\sqrt{D}$ , where  $D$  is the diffusivity (equal to  $1/\sigma\mu$  in the electromagnetic case).

As with other diffusion problems, the general EMI response when the object is placed in a magnetic field which is then suddenly removed can be expressed as a sum of modes whose amplitudes decay exponentially in time at rates that depend on the size, shape and composition of the object and on the spatial structure of the respective modes. The more rapidly decaying modes correspond to proportionally smaller spatial scales of variation. The modes (eigenfunctions) for spheres and cylinders are Bessel functions and solutions can be obtained fairly easily [18]. A sphere of radius  $a$  and relative permeability  $k$  in a static magnetic field  $\mathbf{H}_0$  will have an induced magnetic dipole moment  $\mathbf{m}$  in the direction of the field with strength given by

$$(20) \quad m_0 = 2\pi a^3 H_0 \frac{2(k-1)}{k+2}.$$

When the field is sharply cut off, the induced moment decays according to

$$(21) \quad m(t) = 2\pi a^3 H_0 \sum \frac{6k \exp(-\delta_n^2 t / \sigma\mu a^2)}{(k+2)(k-1) + \delta_n^2},$$

where  $\sigma$  and  $\mu$  are the electrical conductivity and magnetic permeability of the sphere. The eigenvalues  $\delta_n$  are the roots of

$$(22) \quad \tan(\delta) = \frac{(k-1)\delta}{k-1+\delta^2}.$$

The diffusion of heat from a sphere immersed in a cooling bath of well-stirred fluid behaves in essentially the same way [17, §9.6]. In that case, the heat  $Q$  stored in the sphere decays as

$$(23) \quad Q(t) = \frac{4}{3}\pi a^3 \rho c T_0 \left\{ \frac{\eta-1}{\eta+2} + \sum \frac{6 \exp(-\kappa\delta_n^2 t / a^2)}{(\eta+2)(\eta-1) + \delta_n^2} \right\},$$

where now  $\kappa$  is the thermal diffusivity,  $\rho$  is the density,  $c$  is the specific heat and  $T_0$  is the initial temperature of the sphere. The parameter  $\eta$ , which replaces  $k$  in equation (22) is determined by the relative heat capacities  $C$  of the sphere and the surrounding fluid,

$$(24) \quad \eta = \frac{3C_{sphere} + C_{fluid}}{C_{fluid}}.$$

Although the similarity between the solutions of the electromagnetic and heat (or mass) diffusion problems should not be surprising, it is revealing. The early time behavior expressed by equation

(15) is also observed in the conventional diffusion situations [16, §6.3.3]. In particular the transition from  $t^{-1/2}$  to  $t^{-3/2}$  behavior is not unique to the electromagnetic problem.

The  $t^{-3/2}$  regime is not present in the transient EMI response of nonmagnetic ( $k = 1$ ) objects. This is not an issue of magnetic vs. non-magnetic per se, but rather a general aspect of diffusion involving finite bodies. Referring back to equation (21), the modal time scales are increasing functions of the object's magnetic permeability. On the other hand, the  $t^{-1/2}$  to  $t^{-3/2}$  crossover time is a decreasing function of permeability [6]. With a nonmagnetic object the exponential character of the decay is manifested before the transition can occur. The same situation arises in the heat conduction problem described by equation (23) when the heat capacity of the sphere is not large compared to the heat capacity of the surrounding fluid.

## Relaxation Rate Distributions

The frequency domain response (16) corresponding to the early time regime is a special case of the Cole-Cole formula for dielectric polarizability [19, 20, §3.7]

$$(25) \quad \varepsilon(\omega) = \varepsilon_\infty + \frac{\varepsilon_0 - \varepsilon_\infty}{1 + (i\omega\tau_0)^{1-c}}$$

where  $\varepsilon$  is the dielectric polarizability and  $\varepsilon_0$  and  $\varepsilon_\infty$  correspond to the limits  $\omega \rightarrow 0$  and  $\omega \rightarrow \infty$ . The Cole-Cole diagram is a parametric plot of the quadrature (imaginary part) vs. the in-phase (real part) frequency response. Figure 16 shows examples. The symbols are quadrature and in-phase components of the three principal axis polarizabilities of a munitions fragment recovered from the Badlands Bombing Range. Lines show the Cole-Cole formula fit to the data. The surface mode time scale sets the frequency of the peak quadrature response ( $Q_{\max}$ ), while the parameter  $c$  is related to surface mode bandwidth.  $c = 0$  for a loop and  $1/2$  for a steel sphere.

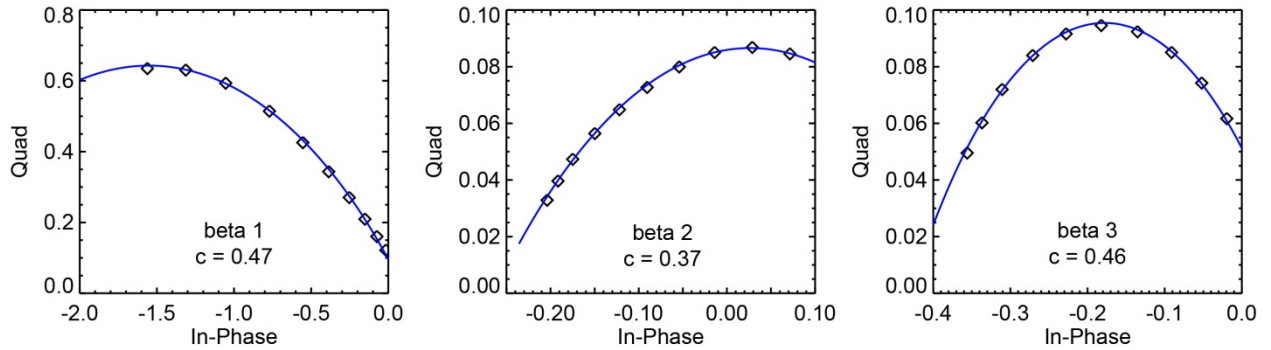


Figure 16. Cole-Cole diagrams of principal axis polarizabilities for a munitions fragment recovered from the Badlands Bombing Range.

We have observed that this general Cole-Cole formula can represent the frequency domain EMI responses of a variety of compact metal targets with values of  $c$  typically ranging from 0 to

around  $1/2$  depending on the object [1, 7]. Wei et al [21] have also noted that the dielectric response of materials has similar characteristics to the EMI frequency response.

The response of composite objects can also be expressed using the Cole-Cole representation. This is illustrated in Figure 17 for 37mm projectiles with and without driving bands. The plot on the left is for axial excitation and the plot on the right is for transverse excitation. Red circles show the measured response for an intact round and black diamonds show the response for a round with its driving band missing. The Cole-Cole model with  $c \sim 1/2$  fits both the axial and transverse response of the 37mm without its driving band (solid curves). The driving band alters the axial response, adding a loop-like response at low frequency (dashed curve). Miller et al [7] noted this loop-like contribution from driving bands on the frequency domain response of various projectiles.

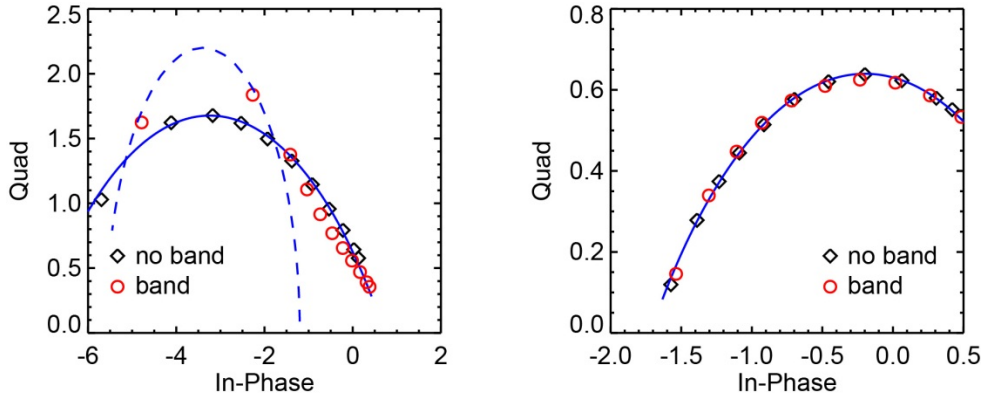


Figure 17. Cole-Cole plots for 37mm projectiles excited axially (left) and transversely (right). Red circles correspond to an intact round, black diamonds to a round with its driving band missing.

A Cole-Cole relaxation process has a continuous distribution of exponentially decaying components with distribution  $g(\tau)$  of relaxation rates  $\alpha = 1/\tau$

(26)

$$g(\tau) = \frac{\sin(\pi c)}{\cosh((1-c) \ln(\tau/\tau_0)) - \cos(\pi c)}.$$

The EMI response in equation (21) is sum of discrete exponential modes with amplitudes  $\hat{g}_n$  given by

(27)

$$\hat{g}_n = 2\pi a^3 H_0 \frac{6k}{(k+2)(k-1) + \delta_n^2}$$

where the  $\delta_n$  are roots of equation (22). Figure 18 compares the Cole-Cole relaxation time distribution  $g(\tau)$  with the modal amplitude distribution  $\hat{g}_n$  for a 2" diameter steel ball. In plotting  $g(\tau)$  we include a factor  $\sqrt{\tau}$  to account for the  $\Delta(1/\tau_n)$  factor relating sums and integrals of the

relaxation rate  $\alpha = 1/\tau$ , and  $g(\tau)$  has been scaled to correct for the difference between Cole-Cole and standard sphere response normalizations. The shapes of the distributions are identical. The only difference is that the sphere has the discrete spectrum shown by blue diamonds, while the Cole-Cole process has a continuous spectrum shown by the black curve.

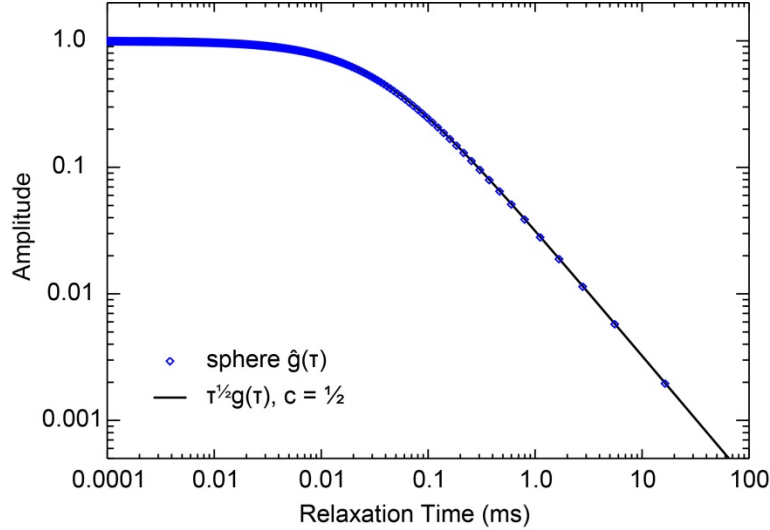


Figure 18. Cole-Cole relaxation time distribution compared with model amplitude distribution for a 2" diameter steel sphere.

There is no essential difference between  $g$  and  $\hat{g}$  in the surface mode regime, and as illustrated by Figure 19, the Cole-Cole approximation reproduces exact theory for a steel sphere through that regime. The discrete mode effects are only seen at late times, while an essentially continuous distribution of modes needed to sustain the algebraic decay at very early times.

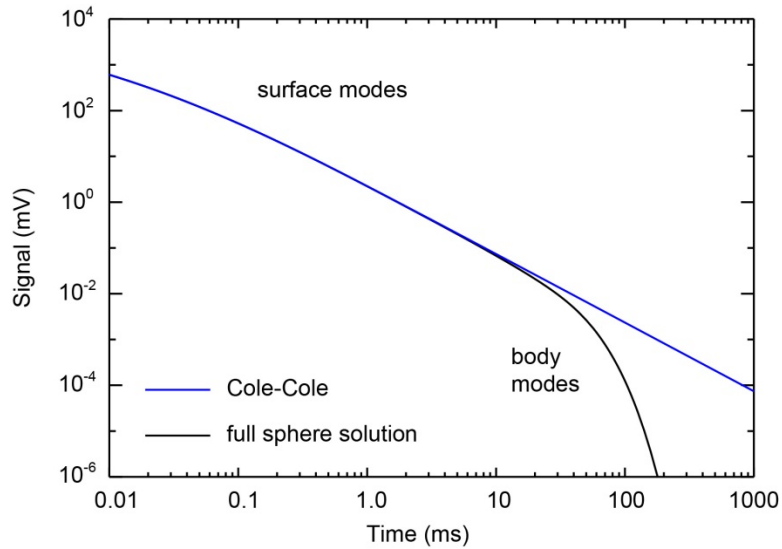


Figure 19. Calculated 2 inch sphere response compared to Cole-Cole approximation.

We have considered the utility of using Prony decomposition [22] to fit the principal axis polarizabilities of measured EMI responses to sums of decaying exponentials. Examples are shown in Figure 20, for a 60mm mortar on the left and an exploded 4.2" mortar body (half-shell) on the right. Upper plots show Prony model fits to the principal axis polarizabilities and lower plots show the corresponding relaxation time distributions. The measured polarizabilities are shown by the black curves which end up bouncing around at the noise floor. Prony model fits are shown by the colored curves, which are extrapolated below the noise floor using dashed lines. Typically only 4-5 terms are required to fit the data over the measured decay range. The amplitudes of the exponential terms fall off roughly as  $1/\tau$ , consistent with the asymptotic decay range in Figure 18. Prony decompositions were done for polarizabilities calculated from all of the former Camp San Luis Obispo munitions and clutter signatures (Table 3 and Table 4). They all look pretty much the same. The main differences among targets are in the overall strength of the response and the fundamental mode time scale. Figure 21 is a scatter plot of response strength vs. fundamental mode time scale for these targets. We have not found the results to be particularly informative. Basically we have a simple curve fit which tends to obscure the physics of the early time response.

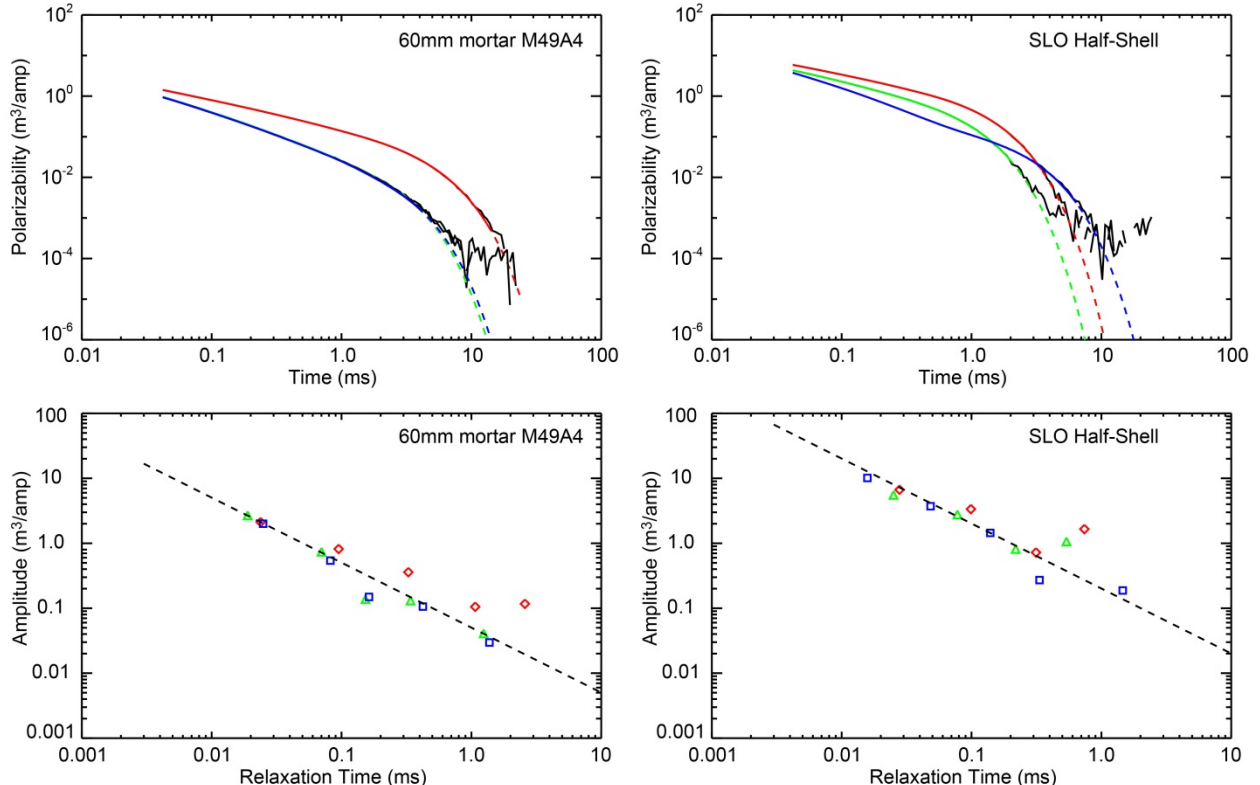


Figure 20. Empirical decay time spectra for 60mm mortar (left) and exploded 4.2" mortar body (right). Top plots show Prony model fits to principal axis polarizabilities, bottom plots show corresponding relaxation time distributions.

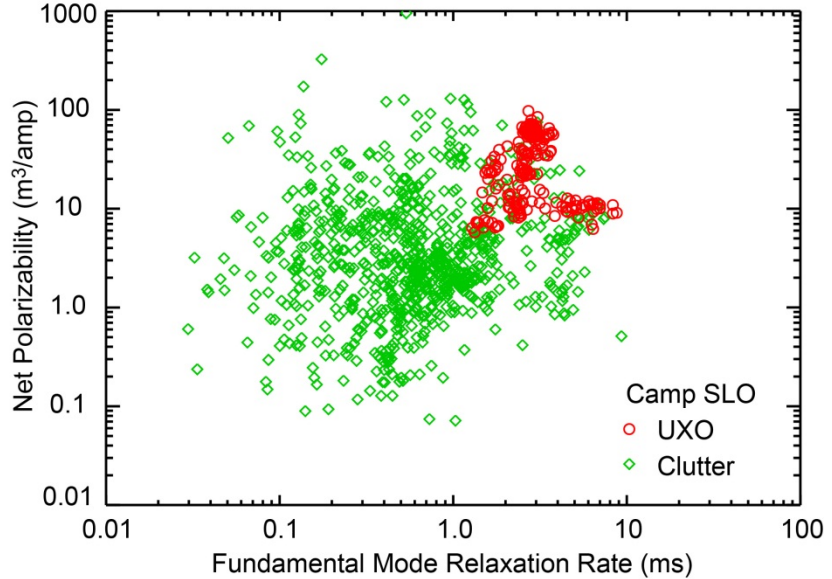


Figure 21. Scatter plot of response strength vs. fundamental mode relaxation rate from Prony fits to munitions and clutter polarizabilities.

### Decay Time Effects on Classification Performance

In its normal data acquisition configuration the TEMTADS array measures the EMI decay averaged over logarithmically spaced time intervals out to 25 ms after the primary field pulse. A significant fraction of the response at the earlier times is due to ringdown of the electronics and coils after the primary field is cut off. Figure 22 shows the response for several different receiver coil configurations used in the TEMTADS array and its man-portable and hand-held adjuncts [13]. The data analyzed in this project were collected using the standard TEMTADS array with 25 cm square receive coils. This background response must be subtracted to get the target's EMI response. However, the background response tends fluctuate with changes in the ambient temperature and other environmental factors, which adds noise to the measured EMI response of the target. In the field, we typically take background shots every half hour or so. Figure 23 shows the TEMTADS background variability observed while working at several field sites. At early times this noise is caused by ringdown variability, which decays fairly rapidly with time after the primary field cuts off. At later times the noise is dominated by ambient electromagnetic fluctuations. The observed  $1/\sqrt{t}$  falloff is consistent with logarithmically gated uncorrelated noise.

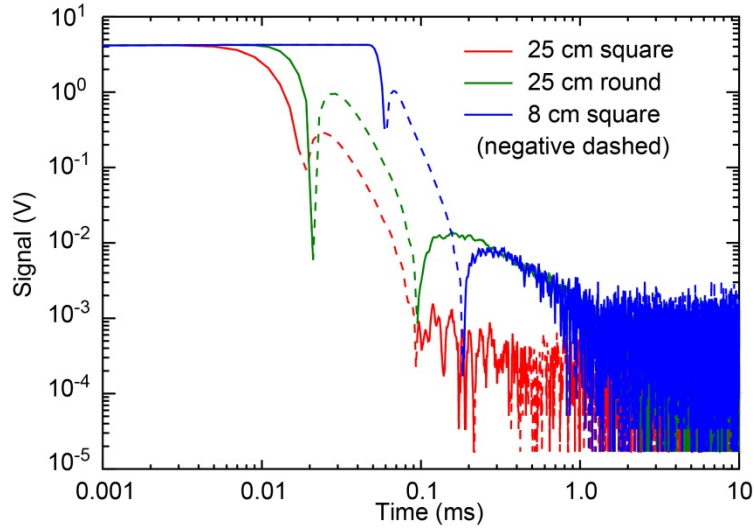


Figure 22. Ringdown for different TEMTADS receiver coils

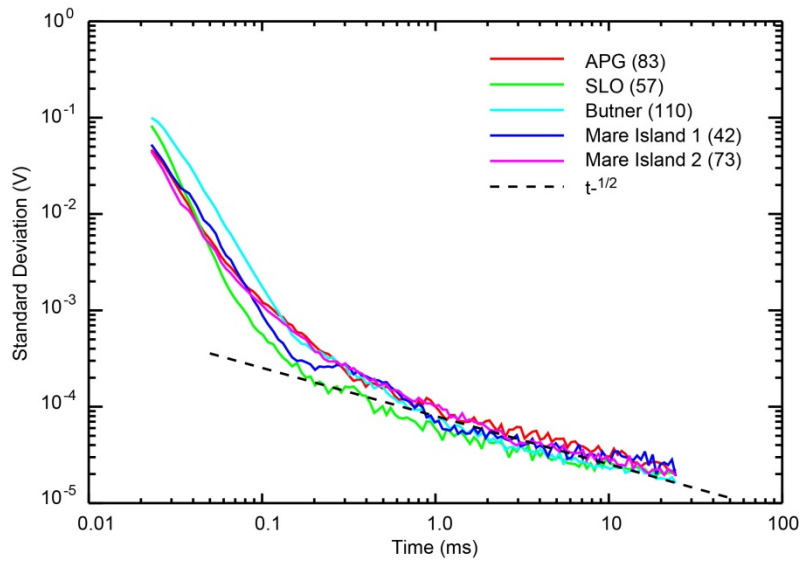


Figure 23. Observed TEMTADS background variation at several sites.

At early times the signal due to a target's EMI response is decaying algebraically with a power law somewhere between  $-1/2$  and  $-3/2$ , more slowly than the noise. At late times the decay varies from  $t^{-3/2}$  to exponential, more rapidly than the noise. Thus it is likely that for at least some targets the signal will be obscured by noise at early and/or late times. Figure 24 shows signal and noise histograms for targets and background shots at 0.1, 1.0 and 10 ms. The data were collected with the man-portable TEMTADS at the 2011 Camp Beale classification demonstration. The distributions are fairly well separated at 0.1 ms, overlap a bit more at 1 ms and overlap considerably at 10 ms. Clearly the late time response data can be significantly corrupted by noise. The question is how important this effect is for classification performance.

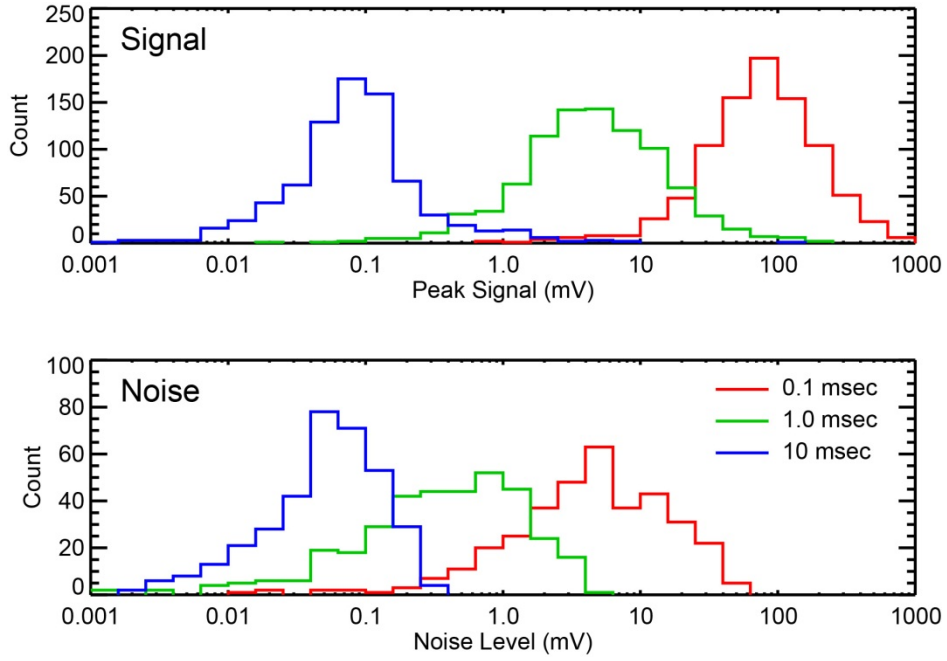


Figure 24. Signal and noise histograms at 0.1, 1.0 and 10 ms for the man-portable TEMTADS at Camp Beale.

We used the signature library to address this question. We used the standard library matching classification procedure [13, §6.4] on polarizabilities calculated from all of the former Camp San Luis Obispo munitions and clutter signatures (Table 3 and Table 4), varying the decay time range. These data were collected in air with the targets in on a test stand below the TEMTADS array, with target/sensor separations chosen to give good strong signals. We should be seeing the effects of decay time range on how similar the munitions and clutter signatures appear rather than the effect of noise on the comparison. Figure 25 shows the results in the form of Receiver Operating Characteristic (ROC) curves. The ROC curve traces performance in terms of munitions items correctly classified vs clutter items as a classification threshold is varied. The standard decay range is 0.04-25 ms. The plot on the left shows how performance varies as the lower limit is increased from 0.04 ms to 2 ms. The plot on the right shows how performance varies as the upper limit is decreased from 25 ms to 1 ms. At the low end performance degrades with  $>0.1$  ms early time cutoff, while at the high end performance degrades with  $<2.5$  ms decay time. Referring back to Table 6, this pretty much corresponds to the surface mode regime for targets of interest. A fortiori this range also corresponds to the signal-to-noise ratio (SNR) “sweet spot” in Figure 24.

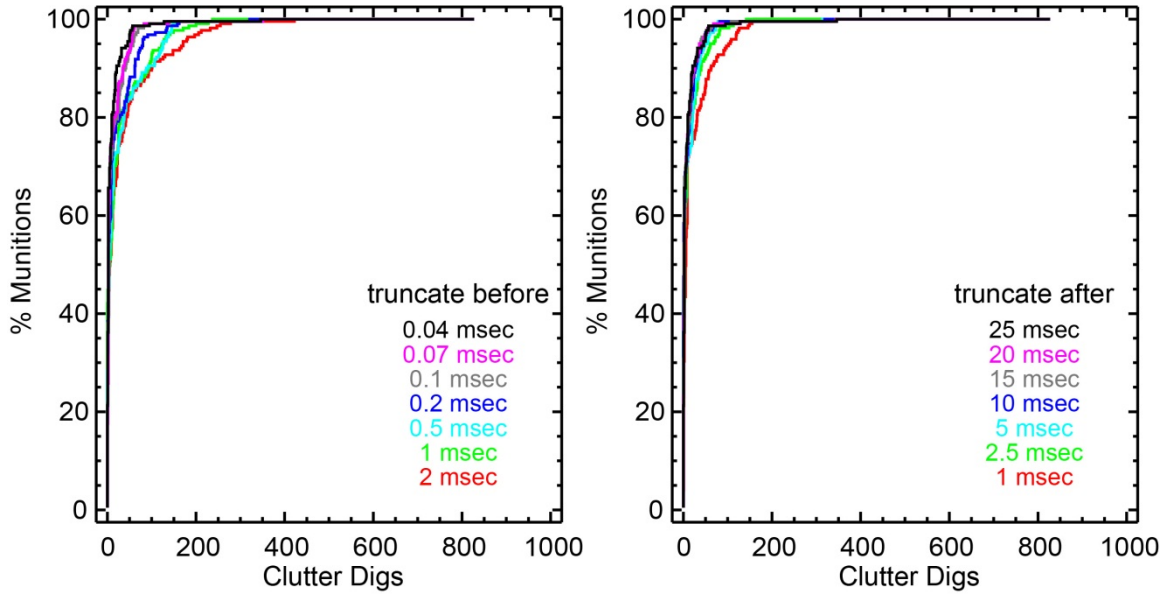


Figure 25. Classification performance using restricted decay time ranges.

Library matching methods employing various procedures to compare polarizabilities of unknown targets with those of targets of interest are commonly used for classification. In general, library polarizabilities derived from signature data collected with sensors using different pulse lengths will not be exactly the same. The measured response may be distorted due to interfering signals from leading and trailing edges of pulses in the Tx sequence. This is referred to as run-on. The effect of shortened pulse length is illustrated in Figure 26, which compares the measured response of a 4 inch diameter aluminum ball with different transmit sequence pulse lengths. The expected signal for a perfect step response is shown with the dashed curve. In this case, the 8.3 ms and 2.8 ms pulses do not capture the complete response. In general, the pulse length required to approximate the ideal (step response) polarizability depends on the target. Recall that there are two time scales for a target's response – the surface mode time scale  $t_S$  associated with the  $t^{-1/2}$  to  $t^{-3/2}$  decay transition and fundamental body mode time scale  $t_B$  corresponding to the late stage exponential decay. Both scale in proportion to size<sup>2</sup>. The body mode time scale is also proportional to the permeability, so steel objects require longer pulses than nonmagnetic ones. Table 6 lists the time scales for various objects. Sensors using pulse lengths shorter than these need to have their own library which includes the distortion due to the run-on effect.

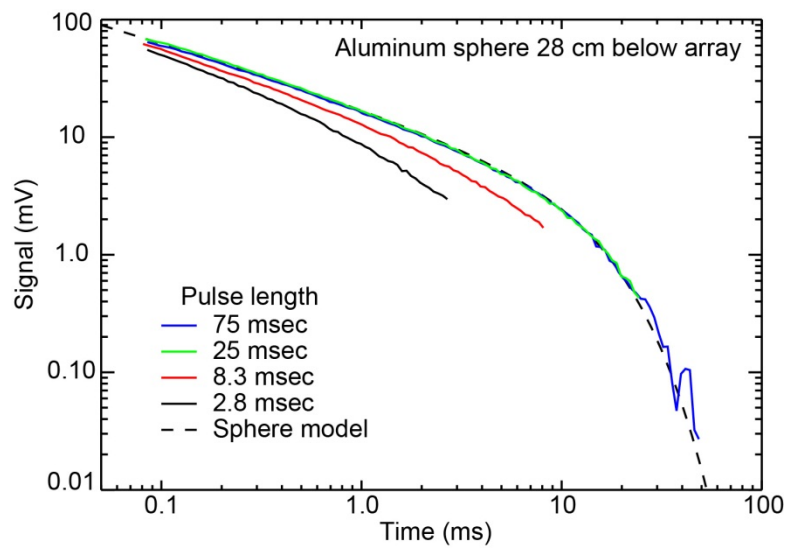


Figure 26. Run-on effect of shortened pulse length on target signature.

## **Conclusions and Implications for Future Research/Implementation**

We have assembled a substantial library of EMI signatures of munitions and clutter which has proven to be quite useful for research purposes and to support development of classification procedures. As new, site-specific inert munitions and clutter items become available through the ESTCP live site demonstrations they should be measured and included in the library.

The results shown in Figure 25 indicate that a decay time interval of about 0.1 ms to 3 ms is adequate for classification. All of the data in our library were collected with decays to 25 ms. Some signals are distorted by run-on effects with shorter transmit pulses, so a degree of caution should be exercised when using the library with shorter-decay data.

Typical library matching procedures used today only ask how much a given target looks (in the EMI sense) like a target of interest. Since we now have an extensive library of polarizabilities not only for a variety of representative munitions items but also thousands of clutter items recovered from a number of different munitions response sites. Using this database we can ask whether an unknown target is more munitions-like or more clutter-like, which should improve classification performance. The library-based classification schemes using this approach should be studied in order to determine whether or not they offer improved performance.

## Literature Cited

1. Thomas H. Bell, Bruce J. Barrow and Jonathan T. Miller, "Subsurface discrimination using electromagnetic induction sensors," *IEEE Trans. Geoscience and Remote Sensing*, vol. 39, no. 6, pp. 1286-1293, June 2001.
2. D.A. Steinhurst, G.R. Harbaugh, J.B. Kingdon, T. Furuya, D.A. Keiswetter and D.C. George, EMI Array for Cued UXO Discrimination, Final Report ESTCP Project MR-200601, July 2010.
3. Peter B. Weichman, "Surface modes and multipower-law structure in the early-time electromagnetic response of magnetic targets," *Physical Review Letters*, vol. 93, no. 2, 023902, 9 July 2004.
4. William R. Smythe, *Static and Dynamic Electricity*, Third Edition, McGraw-Hill, New York, 1968, 623pp.
5. A. Erdelyi (ed.), *Tables of Integral Transforms*, vol. 1, McGraw-Hill, New York, 1954, §5.3, equation (4).
6. Thomas Bell, Bruce Barrow, Jonathan Miller and Dean Keiswetter, "Time and frequency domain electromagnetic induction signatures of unexploded ordnance," *Subsurface Sensing Technologies and Applications*, vol. 2, no. 3, pp. 153-175, July 2001.
7. Jonathan T. Miller, Thomas H. Bell, Judy Soukup and Dean Keiswetter, "Simple phenomenological models for wideband frequency domain electromagnetic induction," *IEEE Trans. Geoscience and Remote Sensing*, vol. 39, no. 6, pp. 1294-1298, June 2001.
8. George Robitaille, Jane Adams, Chris O'Donnell, Pope Burr, "Jefferson Proving Ground Technology Demonstration Program Summary," 24 May 1999, Army Environmental Center report SFIM-AEC-ET-TR-99030
9. I.J. Won, D.A. Keiswetter, D.R. Hanson, E. Novikova, and T.M. Hall, "GEM-3: A monostatic broadband electromagnetic induction sensor," *J. Environmental and Engineering Geophysics*, vol. 2, no. 1, pp. 53-64, March 1997.
10. Thomas Bell, "Phenomenology and Signal Processing for UXO/Clutter Discrimination," SERDP Project MR-1595 Final Report, August 2009.
11. George, Vivian, Thomas W. Altshuler and Erik M. Rosen, "DARPA background clutter data collection experiment excavation results," Proc. SPIE Conference on Detection and Remediation of Mines and Minelike Targets III, SPIE Vol. 3392, pp. 1000-1011, April 1998.
12. Jonathan T. Miller and Jim Kingdon, "Quantification of UXO variability for target discrimination," UXO/Countermine/Range Forum, Los Vegas, Nevada, July 10-13, 2006

13. James B. Kingdon, Bruce J. Barrow, Thomas H. Bell, David C. George, Glenn R. Harbaugh and Daniel A. Steinhurst, "TEMTADS Adjunct Sensor Systems", ESTCP projects MR-200807 and MR-200909 Final Report, December 2011.
14. L. D. Landau, E. M. Lifschitz and L.P. Pitaevskii, *Electrodynamics of Continuous Media*, Second Edition, Elsevier, New York, 1984.
15. Fangwei Fu and John Bowler, "Transient eddy-current driver pickup probe response due to a conductive plate," *IEEE Transactions on Magnetics*, vol. 42, no. 8, August 2006, pp.2029-2037.
16. John Crank, *The Mathematics of Diffusion*, Second Edition, Oxford University Press, New York, 1980.
17. H.S. Carslaw and J.C. Jaeger, *Conduction of Heat in Solids*, Second Edition, Oxford University Press, New York, 1986.
18. James R. Wait and Kenneth P. Spies, "Quasi-static transient response of a conducting permeable sphere," *Geophysics*, vol. 34, no. 5, October 1969, pp. 789-792.
19. Kenneth S. Cole and Robert H. Cole, "Dispersion and absorption in dielectrics. I. Alternating current characteristics," *Journal of Chemical Physics*, vol. 9, April 1941, pp. 341-351.
20. B.K.P Scaife, *Principles of Dielectrics*, Revised Edition, Clarendon Press, Oxford, 1998.
21. Mu-Hsin Wei, Waymond R. Scott, Jr. and James H. McClellan, "Robust estimation of the discrete spectrum of relaxations for electromagnetic induction responses," *IEEE Transactions on Geoscience and Remote Sensing*, vol. 48, no. 3, March 2010, pp. 1169-1179.
22. Andrei A. Istratova and Oleg F. Vyvenko, "Exponential analysis in physical phenomena," *Rev. Sci. Instrum.*, vol. 70, no. 2, February 1999, pp. 1233-1257.